UNIVERSITÀ
DEGLI STUDI
DI PADOVA

UNIVERSITA’ DEGLI STUDI DI PADOVA

**Dipartimento di Ingegneria Industriale DII**

Corso di Laurea Magistrale in Ingegneria Aerospaziale

# Direct numerical simulation of the erosion of a wall of a turbulent channel

Relatore: Prof. Francesco Picano

Laureando: Alessandro Campice

Matricola: 1179752

Anno Accademico 2019/2020

# Abstract

L'interazione tra fluido e struttura è un problema che, a causa delle non linearità implicite nella sua definizione, risulta in una difficile trattazione, che spesso non ammette soluzioni analitiche. Esso è tuttavia di enorme importanza in molti campi dell'ingegneria per la descrizione di fenomeni distruttivi e non (fracking e frattura idraulica, flutter, sloshing, ecc...). Per quanto riguarda la descrizione dei fenomeni distruttivi, ossia in cui si ha la rottura del solido in analisi, entrano in gioco anche le difficoltà legate alla descrizione della propagazione dinamica della frattura. Le tecniche di analisi numerica più largamente diffuse, infatti, non sono in grado di risolvere quest'ultimo punto. Questo è dovuto al fatto che tecniche quali il metodo degli elementi finiti (FEM) sono sviluppate basandosi su derivate spaziali e non trovano quindi applicazione in prossimità di una frattura, poichè essa è per definizione una discontinuità nelle proprietà del materiale.

In questa tesi si andrà ad analizzare il problema dell'erosione di una parete in un canale turbolento, tramite una simulazione numerica diretta realizzata mediante l'accoppiamento a due vie delle tecniche dei contorni immersi (IBM) e della peridinamica. La scelta di queste due tecniche è motivata dalle loro proprietà intrinseche: il metodo IBM bene si presta alla descrizione dell'evoluzione dei carichi scambiati tra fluido e solido, anche quando posizione e configurazione di quest'ultimo variano nel tempo; la peridinamica d'altro canto, in virtù della sua formulazione non locale, permette di risolvere la propagazione di cricche nel solido senza la necessità di conoscenze pregresse.

L'accoppiamento di queste tecniche risolutive fornirà quindi informazioni circa le modalità e le dinamiche con cui si sviluppa l'erosione della parete; permetterà inoltre una caratterizzazione del materiale in termini di resistenza all'erosione. Nel seguente elaborato, particolare attenzione verrà posta ai carichi scambiati all'interfaccia solido-fluido.

# Contents

# List of Figures

# List of symbols

| | |
|---|---|
| $\beta$ | Volume correction coefficient |
| $\mathbf{b}$ | External loads applyed to the solid body |
| $\mathbf{E}$ | Energy tensor |
| $\mathbf{f}()$ | PW force function |
| $\mathbf{u}$ | Velocity field |
| $\mathbf{x_i}$ | Coordinates for the *i-th* material point |
| $\delta$ | Peridynamic horizon |
| $\delta_D$ | Dirac delta function |
| $\eta$ | Relative position of solid particles in actual configuration |
| $\mu(s)$ | Function accounting for bond's status |
| $\mu, \nu$ | Dynamic and kinematic viscosity |
| $\nu_s$ | Poisson's ratio |
| $\Phi$ | Damage level |
| $\Phi_2, \Phi_3$ | Similarity non-dimensional groups |
| $\rho, \rho_s$ | Fluid's and solid material's density |

| | |
|---|---|
| $\tau_c$ | Critical shear stress |
| $\tau_R, \tau_\mu, \tau_w$ | Reynolds and viscous stress and wall shear stress |
| $\xi$ | Relative position of solid particles in reference configuration |
| $c_0$ | Micro-modulus |
| $E$ | Young's modulus |
| $f^*$ | Dimensionalizing factor for IBM forces |
| $G_0$ | Energy release rate |
| $h_c$ | Channel height |
| $k$ | Von Karman constant |
| $k_d$ | Erosion coefficient |
| $k_s$ | Bulk modulus |
| $p$ | Fluid dynamic pressure |
| $Re$ | Reynolds number |
| $s, s_0$ | Bond stretch and critical bond stretch |
| $u^+$ | Non-dimensional streamwise velocity in internal coordinates |
| $v_{er}$ | Erosion velocity |
| $z^+$ | Non-dimensional wall distance in internal coordinates |

# Acronyms

**CaNS** Canonical Navier-Stokes

**DNS** Direct Numerical Simulation

**ExPS** Explicit Peridynamics Solver

**FEM** Finite Elements Method

**FSI** Fluid Structure Interaction

**IBM** Immersed Boundary Method

**LES** Large Eddies Simulation

**PMB** Prototype Microelastic Brittle

**PW** Pairwise

**RANS** Reynolds Averaged Navier-Stokes

# Chapter 1

# Introduction

Erosion is a process that follows from the interaction between a fluid flow and a solid media in contact with it and it is the main responsible for breaches in dams and embankment dikes [1]. It is a qualitatively well known, spatial multiscale phenomenon characterized by great time scales. Very little, however, is known in terms of numerical description of the problem due to its intrinsic difficulties in an accurate modeling. Indeed, to numerically describe erosion mechanisms, a two-way coupled code in which dynamic crack propagation is taken into account must be developed.

Experimental tests are available and allow to determine the resistance to jet erosion and piping erosion for cohesive soils (JET and HET respectively). They are tests conducted in laboratory or *in-situ* on soil samples, the results of which are the parameters used to rate the sensitivity of the soil to erosion. It becomes clear that, which such a typology of tests, no information about the detailed process and mechanics behind erosion are obtained.

On the other hand, fluid structure interaction (FSI) solvers commonly available describe solid's motion by mean of classical local theories, based on spatial derivatives equations. However, this kind of theories are not suitable for fracture description, unless a previous modeling is available.

This thesis aims to numerically describe the evolution and the mechanics involved in the erosion of a flat plate, which represents a wall in a fully developed turbulent channel. This is done by a mean of a simulation, in which peridynamics and an immersed boundary method are coupled, together with Navier-Stokes equations. Fluid's domain is solved with a direct numerical simulation (DNS). No previous numerical models are thus required. After a complete description of the flow in the channel, an accurate description of the evolution of the erosion of the surface will be achieved and loads exchanged at the fluid-solid interface are going to be deeply analyzed.

The following work is divided in 5 chapters. Initially, an overview about state of the art for erosion and FSI problems will be presented (sections 2.1, 2.2). A numerical description of the methods used will be given in chapter 3: in particular, sections 3.1, 3.2 and 3.3 for what concerns peridynamics, Navier-Stokes equations and Immersed Boundary Methods respectively. The code CaNS-ExPS developed to solve the problem is described in section 4.1, where it is explained the coupling of all numerical techniques already introduced. Section 4.3 gives a precise description of the geometric characteristics of this problem, as well as the parameters used to describe the fluid and the solid body. Finally, results before rupture, as erosion proceeds and a confrontation of obtained data with the predicted trend are in chapter 5.

# Chapter 2

# State of the art overview

## 2.1 Erosion process

Erosion is defined by washing away of grains by mean of a fluid flow in contact with a solid medium, which may end up in failure. It can be internal or external, whether the flow is in contact with the surface of the solid or it is underneath the surface, respectively. Mechanisms to originate erosion are piping erosion, regressive erosion, contact erosion and suffusion.

Since erosion is one of the main causes for failure of dams, in order to prevent them from irreversible damages that will lead to floods and damages, lot of attention is given to the characterization of the erodabiblity of the material. This is done in particular for soils and it is done by mean of experimental tests (HET, JET), in which the rate of eroded material is measured and related to the properties of the flow. Usually 2 parameters are needed to describe the resistance to erosion of a material since, in the most accepted view of the problem, the rate of erosion is proportional to the applied shear stress. This approach to the problem allows for a determination of the time necessary for a structure to fail in averaged terms.

The linear dependence for the rate of erosion was first introduced by Du Boys [2] in the field of bed sediment transportation. Many modifications to its theory have been made since then, adjusting the proportionality coefficient [3] or modifying the linearity of the relation [4]. Einstein [5] proposed a treatment to the problem in which shear stress is abandoned in favor of fluctuations of velocity. However, all these models were formulated empirically for granular soils and no mathematical explanation of the phenomenon was given.

In many models, turbulence of the flow is also taken into account. As a title of example, Shields [6] proposed a model in which the threshold shear stress for non cohesive particles is related to the maximum pressure fluctuations. As for cohesive soils, Briaud et al. [7] related erosion to the fluctuations in shear and normal stress. However subsequent developments and simplifications lead again to a linear proportionality as the one described above.

The most commonly used erosion law [8], experimentally verified under different conditions, is:

$$v_{er} = \begin{cases} k_d(\tau - \tau_c) & \text{if } \tau > \tau_c \\ 0 & \text{otherwise} \end{cases} \tag{2.1}$$

being $v_{er}$ the velocity of erosion, $k_d$ the erosion coefficient and $\tau_c$ the critical shear stress, a threshold value the shear stress has to overpass in order to initialize erosion.

As for numerical modeling of the problem, the first model was developed by Vardoulakis et al. [9] for the determination of sand production in the field of oil extraction. This is, however, only reliable to granular solids.

More recent studies treat erosion with a volume of fluid (VOF) approach [10] to determine the interface of the domains and describe their interaction. However, low resolution is achieved for the properties of the fluid at the interface where the mesh has to be substantially refined.

## 2.2 Fluid Structure Interaction problems

Fluid Structure Interaction (FSI) problems deal with strongly nonlinear multiphysics phenomena that cover a wide range of engineering fields [11]. In general, they are focused on studying the behavior of a solid body interacting with a surrounding or internal fluid flow. These kind of problems are encountered in many different fields of study, from the microscopic scale to the macroscopic one. A typical example of a FSI problem is flutter or, more generally, aeroelasticity [12] which is by definition the result of the mutual interaction between a body and the fluid flowing around it (i.e. a wing of a plane). Some other examples of FSI problems include, but are not limited to, sloshing [13], aerodynamics [14], sedimentation [15], particles motion and bio mechanics [16].

Due to the natural complexity of these problems, very little can be done using only a theoretical approach. In addition, problems such as blood flow in an organism [17] are difficult to be studied also experimentally. All of this led to the development of numerical codes in order to properly investigate these kind of phenomena.

There are mainly 2 possible approaches to a FSI problem: the monolithic and the partitioned one. In the former, fluid and solid dynamics are studied together using a single system of equations. Interface conditions are automatically solved and are implicit in the nature of the problem. On the other hand, the latter solves fluid and solid equations separately. These two must then communicate at their interface and coupling is made possible with interface conditions, that are introduced lately and can vary following the nature of the problem. The main advantage of the partitioned method is that it permits the usage of well known and validated theories when solving both structural and fluid dynamics as they are treated independently from each other. Therefore computational cost can be maintained low. However, this kind of approach lacks in accuracy with respect to the monolithic one which, in contrast, requires a more complex implementation [11].

With the partitioned approach it is clear that solid bodies and fluid domain are required to have different meshes in order to properly solve their specific equations. Again, there are 2 more possibilities: the conforming mesh method and the non-conforming one.

When using a conforming mesh, the interface between the domains is determined by the mesh itself and the position of the interface is considered as part of the solution. As the solution advances, re-meshing is required in order to adapt the grid to the position of the solid body. This is not the case for non-conforming mesh methods where different and independent grids are determined for the solid body and for the fluid. In this case interface conditions and location are introduced in the problem in the form of boundary conditions to be applied to the equations.

Immersed methods represent most of recent developments in FSI field and are an example of non-conforming mesh methods.

As we will discuss later, in this framework the approach is going to be a partitioned approach, since it allows for the usage of arbitrary chosen theories when solving fluid and solid body dynamics. In particular DNS will be used when solving the fluid domain, while peridynamics will analyze solid body motion and determine crack propagation. Immersed boundary method will allow for these two computational techniques to communicate.

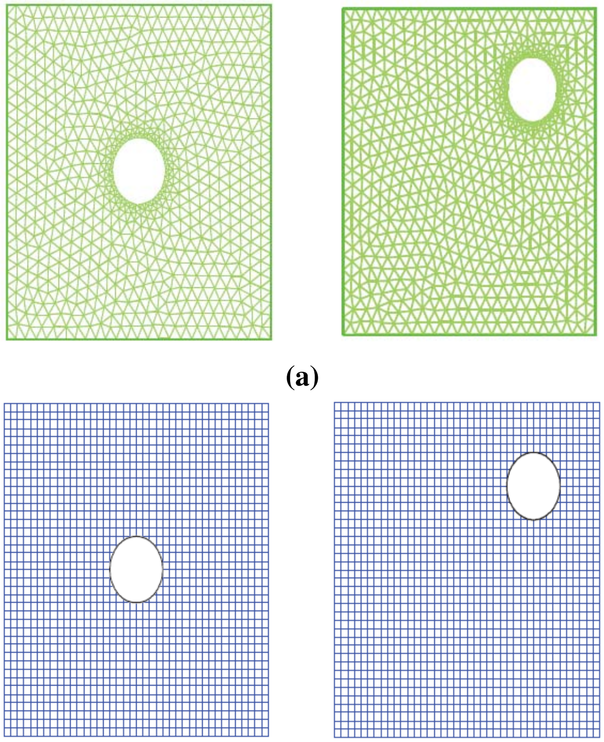

(a)

(b)

**Figure 2.1:** *Examples of a conforming (a) and non-conforming (b) mesh method [11].*

# Chapter 3

# Methodology

## 3.1 Peridynamics

Although being a phenomenon long studied, fracture is still a field of major interest in many engineering fields. First steps in understanding fracture mechanics were made by Griffith [18] during World War I, and then by Irwin [19]. With the advent of computers and the improvement in their capabilities, many structural solvers have been developed, but still simulation of crack propagation is a challenging issue.

### 3.1.1 An introduction to peridynamics

By definition, a crack is a discontinuity in a solid medium and therefore it represents a problem when trying to study it with classical mechanics, such as Finite Elements Method (FEM) [20]. Indeed, problems encountered are related to the fact that equations of motion in this kind of method are based on spatial derivatives and therefore discontinuities can not be solved with a similar formulation. Across the years many alternative ways of treating the problem have been proposed and they mostly consist of modifications of numerical methods based on classical mechanics. Cohesive crack models [21] can be introduced together with the usage of interface elements to solve the equation of motion in the proximity of discontinuities [22] - [23]. However it is required to know *a priori* how the path of the discontinuity evolves. An alternative method is the eXtended Finite Element Method (XFEM), in which some additional functions are added in order to predict the crack propagation [24]. This way of proceeding results in a difficult implementation, especially in 3D cases.

Only in recent years an innovative method called Peridynamics has been proposed [25]. The peculiarity of this theory is that it does not use strain in its formulation. It is therefore built around integral equations instead of differential ones and, as a consequence, crack propagation can be easily studied. In addition, this is a meshfree particle method as it deals only with a discrete number of particles to describe the state of the system. This represents a great advantage when studying fracture since mesh constraint dependencies are eliminated and there is no need for remeshing as the crack propagates. As we will see, the only limitations for this method are related to its computational cost which is higher than FE methods.

Peridynamics has been used in a wide variety of fields, showing surprisingly good results. First publication about numerical simulations using this technique has been made by Silling and Askari 155 , in which they studied convergence in fracture simulation problems with brittle materials and the effect of the impact of a sphere on a plate. Ha and Bobaru [26] - [27] were able, by mean of this computational method, to explain the asymmetry of a crack path in a symmetrical domain, reproducing previously obtained experimental results. Agwai et al. [28] conducted a confrontation between the resolutive methods discussed above (XFEM, cohesive zone models and peridynamics). Further developments of the peridynamic model allowed to apply this numerical technique also to the field of composite materials. This is possible with the introduction of fiber bonds, matrix bonds and interply bonds [29] - [30]. Another way to study composite materials proposed by Kilic et al. [31] uses a random number generator to predict fiber position in a reinforced lamina. They then studied fracture propagation in center cracked lamina with fibers oriented at different angles. With peridynamics it is also possible to account for fatigue phenomena by progressively reducing some critical parameters used for the characterization of the material [32].

Peridynamics, from greek “peri” (around) and “dynami” (force), is a non-local theory of continuum in which material points are thought to interact with a whole set of points within a certain distance called peridynamic horizon [33]. Its earliest formulation, called Bond Based Peridynamics, allows for the description of brittle materials. A more general formulation that include a wider class of materials is under the name of State Based Peridynamics.

In the following we will address only to Bond Based Peridynamics.

### 3.1.2 Equations of motion

As already said, peridynamics is a non local continuum theory that treats a solid medium as an ensemble of material points interacting between each other, even if not adjacent. In the bond based formulation, interactions between couples of material points are referred to as bonds and the maximum distance among which they can interact is the perydinamic horizon $\delta$. All particles closer than $\delta$ from a material point (i.e. all particles with whom it can interact) represent its neighborhood.

Let $\rho_s$ be the density of the material of which the continuum $R_0$ is made [20], then for every material point of coordinates $\mathbf{x}_i$ the equation of motion can be written as:

$$\rho_s \frac{d^2\mathbf{x}_i}{dt^2} = \int_{H_i} \mathbf{f}(\mathbf{u}(\mathbf{x},t) - \mathbf{u}(\mathbf{x}_i,t), \mathbf{x} - \mathbf{x}_i) dV_x + \mathbf{b}_i \tag{3.1}$$

in which $H_i = \{\mathbf{x} \in R_0, ||\mathbf{x} - \mathbf{x}_i < \delta\}$ is the neighborhood of the considered material point, the function $\mathbf{f}$ is the pairwise force function (PW) and the vector $\mathbf{b}_i$ is representative of external forces acting on the body per unit volume at the time instant t. PW force function is representative of the force density per unit volume squared exchanged between material points of coordinates $\mathbf{x}$ and $\mathbf{x}_i$.

In bond based formulation, each interaction between material points is independent from each other and it occurs along bonds. Therefore, PW force function

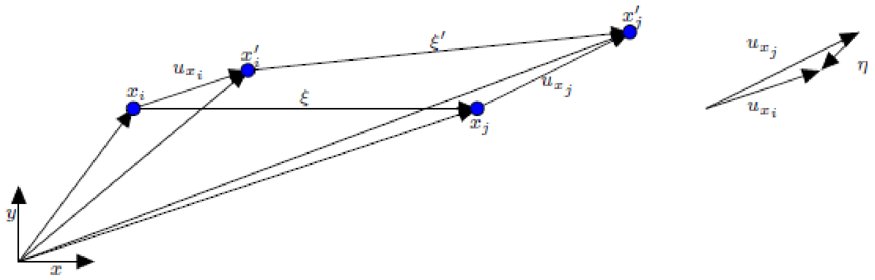

**Figure 3.1:** *Graphical representation of relative initial position $\xi$ and relative displacement $\eta$ between solid particles $x_i$ and $x_j$ [34]*

can be shown to depend only upon the relative position of material points in their reference configuration $\xi$ and their relative displacement in actual configuration $\eta$.

$$\boldsymbol{\xi} = \boldsymbol{x}_0 - \boldsymbol{x}_{i0} \tag{3.2}$$

$$\boldsymbol{\eta} = (\boldsymbol{x}_t - \boldsymbol{x}_0) - (\boldsymbol{x}_{it} - \boldsymbol{x}_{i0}) \tag{3.3}$$

What said is valid for so called prototype microelastic brittle (PMB) materials, for which PW force function can be derived from a potential and it is in the form of an elastic force in classic mechanics:

$$\mathbf{f} = \mathbf{f}(\boldsymbol{\xi}, \boldsymbol{\eta}) = c_0 s \mu(s) \frac{\boldsymbol{\xi} + \boldsymbol{\eta}}{||\boldsymbol{\xi} + \boldsymbol{\eta}||}. \tag{3.4}$$

$$s = \frac{||\boldsymbol{\xi} - \boldsymbol{\eta}|| - ||\boldsymbol{\xi}||}{||\boldsymbol{\xi}||} \tag{3.5}$$

The parameter $c_0$ in this formulation is called micro-modulus and it is the stiffness of the bond, $s$ is the stretch of the bond and $\mu(s)$ is a function that accounts for bond fracture. Thinking of 3.4 as an elastic force, $c_0$ would be the stiffness of a spring. In this particular formulation it is assumed to be constant over time and position, but a dependence upon this characteristics, thus anisotropy, may be included [35].

In bond based peridynamics, fracture is thought to evolve from bond rupture which occurs only when the stretch of a bond overcomes a threshold value, denoted as critical stretch $s_0$. Once a bond is broken, it can no more transmit any load. Hence, $\mu(s)$ is a history-dependent scalar valued function that introduces this last consideration in PW force function formulation:

$$\mu(s) = \begin{cases} 1 & \text{if } s < s_0 \\ 0 & \text{otherwise} \end{cases} . \tag{3.6}$$

It's important to notice that bonds only break in tension (i.e. $s > 0$) and can not break when in compression.

### 3.1.3 PMB material characterization

There are only 2 parameters needed to completely describe a PMB material: $c_0$ and $s_0$. Different formulations for these two can be done, depending on the characteristics of the problem: plane stress or plane strain (2D problems) or 3D. In all cases, expressions are derived from energetic considerations at microscopic and macroscopic scale.

Consider a large 3D homogeneous body under isotropic tension so that every material point undergoes the same tensile condition. The strain energy density computed at microscopic scale under peridynamics assumptions must equal the one computed from classical mechanics [36].

In particular, denoting $\eta = |\boldsymbol{\eta}|$ and $\xi = |\boldsymbol{\xi}|$, under these assumptions we will have $\eta = s\xi$ anywhere. It follows that the modulus of PW force between 2 arbitrary particles is $f = c_0 s = c_0 \eta/\xi$. The energy stored in the body per unit volume (i.e. the strain energy density) is derived from:

$$W = \int_{H_i} w dV_i = \int_0^\delta \left(\frac{1}{2} f \eta\right) 4\pi\xi^2 d\xi = \frac{\pi c_0 s^2 \delta^4}{4} \tag{3.7}$$

where $w = f\eta/2$ is the micro elastic potential associated to a single bond (i.e. the work required to stretch a single bond from $\xi$ to $\eta$ under isotropic extension).

The value computed from 3.7 must equal the strain energy density deriving from linear elastic theory $W = 9k_s s^2/2$. Equating these expressions and solving for the micromodulus $c_0$ yields to:

$$c_{0,3D} = \frac{18k}{\pi\delta^4}. \tag{3.8}$$

Critical stretch $s_0$ can then be computed from the work required to break all the bonds per unit fracture area for a brittle material. This is, following peridynamics:

$$G_{0,3D} = \int_{S_0} w_0 dS = \frac{\pi c s_0^2 \delta^5}{10} \tag{3.9}$$

$$w_0 = \int_0^{s_0} f d\eta \tag{3.10}$$

in which $S_0$ is the fracture surface and $w_0$ is the work associated to the breakage of a single bond. $G_0$ is the energy release rate and it is a measurable quantity for brittle materials. It is also a parameter widely used in other fields of research and it was first introduced by Griffith. It follows that an expression for $s_0$ can be obtained simply from 3.9:

$$s_{0,3D} = \sqrt{\frac{5G_0}{9k_s\delta}}. \tag{3.11}$$

In a similar way it is possible to express the micromodulus $c_0$ and the critical stretch $s_0$ for plane strain and plane stress cases. For the sake of completeness, all 3 formulations are reported below [37]:

$$c_0 = \begin{cases} \frac{9E}{\pi h\delta^3} & \text{for 2D plane stress} \\ \frac{48E}{5\pi h\delta^3} & \text{for 2D plane strain} \\ \frac{12E}{\pi\delta^4} & \text{for 3D} \end{cases} \tag{3.12}$$

$$s_0 = \begin{cases} \sqrt{\frac{4\pi G_0}{9E\delta}} & \text{for 2D plane stress} \\ \sqrt{\frac{5\pi G_0}{12E\delta}} & \text{for 2D plane strain} \\ \sqrt{\frac{5G_0}{9k_s\delta}} & \text{for 3D} \end{cases} \tag{3.13}$$

Attention must be payed when defining material properties for a PMB material. Indeed, as we already said, material points interact only between couples. This defines a so called Cauchy crystal for which Poisson ratio $\nu_s$ is limited in value as it necessarily is $\nu_s = 0.25$ [38]. This limitation is overpassed in state based peridynamics where every value for $\nu_s$ is suitable.

### 3.1.4 Damage level and crack evolution

From what said in the previous section it is possible to determine how a body will eventually break. Breakage will occur in different steps, having the separation of a particle when all the bonds with all points within its horizon break. Therefore it is possible to have a configuration where only some of the bonds break, so that there is not a complete separation of the particle itself. We can therefore define a damage level for a material point of coordinates $\mathbf{x}_i$ at time instant t as:

$$\Phi(\mathbf{x}_i, t) = 1 - \frac{\int_{H_i} \mu(\mathbf{x}_i, t, \xi) dV_x}{\int_{H_i} dV_x}. \tag{3.14}$$

Following this definition, complete separation occurs only when $\Phi = 1$, while $\Phi = 0$ represents virgin material.

## 3.2 Navier Stokes equations for a turbulent flow

The equations used to describe the behavior of an incompressible flow ($\rho = cost.$) are the continuity equation and the momentum equation [39]-[40]:

$$\nabla \cdot \mathbf{u} = \mathbf{0} \tag{3.15}$$

$$\frac{D\mathbf{u}}{Dt} = -\frac{1}{\rho} \nabla p + \nabla \cdot (2\nu \mathbf{E}) \tag{3.16}$$

in which $\mathbf{u}$ represent the velocity of the fluid, $\nu$ its kinematic viscosity, p its pressure and $\mathbf{E}$ is a 3x3 tensor called the energy tensor:

$$\mathbf{E} = \frac{1}{2}(\nabla\mathbf{u} + \nabla\mathbf{u}) \tag{3.17}$$

This set of equations holds both for turbulent and non turbulent flows, however when dealing with turbulence it's usually convenient to further develop the momentum equation. Since turbulence is a non stationary and chaotic phenomenon, we can refer to the instantaneous variables involved in the problem as a sum of a mean part and deviations from the mean, or fluctuations. When considering mean fields only, symmetries of the problems lost by the effect of turbulence are brought back. It is therefore possible to substitute all the variables in Navier-Stokes equations ($\mathbf{u}, \nu, \mathbf{E}$) with their relative Reynolds decomposition, obtaining:

$$\nabla\cdot < \mathbf{u} >= 0 \tag{3.18}$$

$$\frac{D < \mathbf{u} >}{Dt} = -\frac{1}{\rho}\nabla < p > +\nabla\cdot(2\nu < \vec{\vec{E}} >) - \nabla\cdot\boldsymbol{\tau_R} \tag{3.19}$$

$$\vec{\vec{\tau}}_R =< \mathbf{u}' \cdot \mathbf{u}'^{\mathbf{t}} > \tag{3.20}$$

where fluctuations are evidenced by a superscript and the mean fields by $<>$.

The only difference with respect to the previous set of equations is the presence of the Reynolds stress tensor $\boldsymbol{\tau_R}$. If the fluid was stationary (non turbulent), the terms $\mathbf{u}'$ would be null, thus obtaining again 3.16. This additional term can be interpreted as an extra stress exerted by the turbulent fluctuations on the mean field. It is though important to notice that, despite the name, it is not an effective stress as it could be better described as an additional momentum flux due to the turbulent motion of the fluid. Its magnitude is usually nonzero, being greater than viscous stress except for near wall regions, where the latter becomes predominant.

### 3.2.1 Resolutive methods

**DNS**

Due to strong non linearity of the problem, it is not possible to compute any analytical solution, so that numerical methods are needed [41]. The most intuitive resolutive method consists of discretizing Navier-Stokes equations (3.15 - 3.16) over the fluid domain. This technique is called Direct Numerical Simulation (DNS). Its limitations are related to computational time, being this method very expensive. Indeed, to properly solve the fluid domain it is required to take into account all the processes present in turbulence. This reflects the need of having cell sizes comparable to the smallest fluid scale, the Kolmogorv scale $\eta$.

Denoting the characteristic size of the problem as L and the grid spacing as $\Delta x$, the number of points needed along the x direction is $N_x = L/\Delta x$. From Kolmogorov's theory, the turbulent kinetic energy dissipation rate and the Kolmogorov scale can both be related to scale entities, being respectively:

$$\varepsilon \propto \frac{U^3}{L} \qquad\qquad \eta = \frac{\nu^3}{\varepsilon^{1/4}} \tag{3.21}$$

where U is a reference velocity. It follows that, since we must have $\Delta x \propto \eta$, with reference to all 3 dimensions, the number of points needed to properly solve the fluid is:

$$N_p \propto N_x^3 \propto \left(\frac{L}{\eta}\right)^3 = \left(\frac{L}{\nu^3/\varepsilon^{1/4}}\right)^3 \propto \left(\frac{L^4U^3}{L\nu^3}\right)^{3/4} = Re^{\frac{9}{4}} \tag{3.22}$$

As for the discretization time, it is necessary to introduce the Kolmogorov characteristic time $\tau_\eta = \eta/u_\eta = (\nu/\varepsilon)^{1/2}$ and the scale time $T = L/U$ so that the number of time steps required is $N_t = T/\tau_\eta$.

In conclusion, the total simulation time is:

$$T_{tot} \propto N_p \times N_t \propto Re^{11/4} \approx Re^3 \tag{3.23}$$

It follows that DNS is a technique to be employed only with relatively low Reynolds numbers in order to contain the computational cost. As a consequence, it can not be used when trying to solve large scale flows characterized by higher Re, despite the improvements in computers' capabilities of recent years. However, DNS offers full reliability on the results achieved as they are considered as significant as experimental ones, with the further advantage of knowing the whole motion field at any instant.

### RANS

Less expensive methods to solve Navier-Stokes equations when dealing with high order Re are the so-called Reynolds Averaged Navier Stokes (RANS) simulation and Large Eddies Simulation (LES).

RANS simulations are based on averaged Navier-Stokes equations (3.18 - 3.19). The considerations at the base of this resoultive method are that averaged fields vary smoothly, since they do not include fluctuations. Also, as said before, when dealing with mean fields, symmetries are restored allowing for 2D simplifications when the geometry of the problem allows it. The minimum cell size required is then imposed by the gradients of the mean field of motion and it is therefore bigger than in DNS.

Difficulties arise when trying to determine Reynolds stress tensor: it is a symmetric 3x3 tensor, so that RANS consist of 4 equations in 10 unknowns $(u, v, w, p, \tau_{xx}, \tau_{yy}, \tau_{zz}, \tau_{xy}, \tau_{xz}, \tau_{yz})$. This term not being negligible, as it is the only term that distinguishes between a turbulent and a laminar flow, a modeling is required. Indeed, there is no way to estimate velocity fluctuations $u_i'$ without having already solved the problem.

A first attempt to find a suitable solution to the problem comes from Boussinesq, who introduced the concept of turbulent viscosity $\nu_\tau$. Turbulent viscosity differs from viscosity since the former depends on time and position and on the state of motion of the fluid. Following his theory, Reynolds stress tensor $\boldsymbol{\tau_R}$ can be expressed in a similar way of viscous stress tensor **T**:

$$\mathbf{T} = -p\mathbb{I} + 2\mu\mathbf{E} \tag{3.24}$$

$$\boldsymbol{\tau} = -\frac{2}{3}K\mathbb{I} + 2\nu_\tau < \mathbf{E} > \tag{3.25}$$

where K is the turbulent kinetic energy. Substituting this latter expression in 3.19 we obtain the following:

$$\frac{D < \mathbf{u} >}{Dt} = -\nabla < p_m > + \nabla \cdot (2(\nu + \nu_\tau) < \mathbf{E} >) \tag{3.26}$$

$$p_m = \frac{p}{\rho} + \frac{2}{3}K \tag{3.27}$$

in which $p_m$ is called modified pressure. At this point it is necessary to find a way to express $\nu_\tau$. The most common models used to model it are the so called $k-\varepsilon$ and $k-\omega$ but still, they depend on parameters that are function of the particular case to be studied.

### LES

Finally, Large Eddies Simulation (LES) aims to solve the fluid field only up to a certain scale. Indeed, following K41 theory of Kolmogorov, the larger scales are directly influenced by the geometry and the characteristics of the motion itself, while characteristics of the smaller scales are universal as they behave all in the same way and prescind from the particular geometry of the problem. The main idea of this particular technique is to directly simulate the larger scales, whose characteristics are a direct consequence of the geometry of the problem, while the effect of the smaller ones on these ones is modeled.

Since the bigger scales are those that mainly characterize the behaviors of the fluid flow and they are fully resolved, LES correctly consider turbulence and non stationary effects. In that they differ from RANS, where all the effects of turbulence had to be modeled and only the main field, stationary, could be resolved.

It is therefore necessary to define a threshold scale up to which the velocity field will be filtered. We define a filtering operator $G_\Delta$ that allows us to decompose the velocity as $u_i = \tilde{u}_i + u_i'$, where the filtered velocity is $\tilde{u}_i$ and $u_i'$ is the residual velocity. Applying $G_\Delta$ to Navier-Stokes equation we obtain a system of equations similar to that for RANS:

$$\frac{\partial \tilde{\mathbf{u}}}{\partial t} + \nabla \cdot \tilde{\mathbf{u}}\tilde{\mathbf{u}} = -\frac{1}{\rho}\nabla \tilde{p} + \nabla \cdot (2\nu \tilde{\mathbf{E}}) - \nabla \cdot \boldsymbol{\tau}^r \tag{3.28}$$

where $\boldsymbol{\tau}^r$ is the residual stress tensor that has to be modeled. Equation 3.28 is formally identical to 3.19 but they are significantly different in the meaning. Quantities in the latter are tridimensional, chaotic and non-stationary and the only term to be modeled express the effect of the smaller scales on the bigger ones. On the other hand, in RANS, the additional stress tensor has to model the effect of all scales of the fluid and it acts on the averaged fluid field which, in contrary, is stationary.

LES allows for a lower spatial resolution with respect to DNS since smallest scales does not need to be solved. A typical model for $\boldsymbol{\tau}^r$ is Smagorinsky's, which is based on the concept of eddy viscosity.

From what has been briefly said in this section, it is evident that the only resolutive method able to describe a fluid in detail from its larger scale down to the Kolmogorov scale is DNS. Although its time consuming limitations, this technique is to be considered the most accurate and reliable and has to be chosen when a great level of accuracy is required.

## 3.3 Immersed Boundary Method

As briefly discussed in chapter 2.2, the main task concerning a FSI problem is the exchange of informations at the interface between fluid field and solid medium. The Immersed Boundary Method (IBM) is a numerical technique that allows for a simple representation of the problem. Here, the presence of the body is taken into account by mean of additional forces added into the fluid domain in order to mimic no-slip and no-penetration conditions on the surface of the body. In turn, these forces, computed to correctly solve fluid's equation of motion, are the same exerted by the fluid itself on the body and therefore they are used also to solve solid's equations.

IBM was first introduced and developed by Peskin [17]-[42] as a method to study blood flow through a beating heart. Being born in a bio-medical field, after that it has become a widely used method thanks to its versatility and computational efficiency. The particularity of this method is that it uses a fixed in time, structured and spatial uniform grid to discretize the fluid domain, unlike more common resolutive methods where the grid is body-fitted. In time-dependent problems, as material particles move through the computational domain, remesh is therefore not required, thus containing computational cost. Another grid, solidal to the body, will then be introduced to discretize the body itself. It is common to address these two grids as eulerian and lagrangian respectively. Information between the two are exchanged at the interface.

These characteristics make IBM one of the most commonly used methods for the study of particle-laden flows or, more in general, when dealing with complex geometry problems [43].

### 3.3.1 Numerical definition

A particle-laden flow is governed by Navier-Stokes and Newton-Euler equations for what concerns fluid phase and solid particles respectively. Boundary conditions (no-slip and no-penetration) permit to couple these two sets of equations and they enforce the continuity of the velocity at the interface between the phases and the continuity of traction force:

$$u_i^f = u_i^b \tag{3.29}$$

$$\sigma_{ij}^f n_j = \sigma_{ij}^f n_j \tag{3.30}$$

Here superscripts $b$ and $f$ denote solid body entities and fluid related ones respectively.

This condition is achieved with the introduction of a forcing term on the right-hand side of equation 3.16, when in proximity of the body. This new equation is then solved over the entire fluid domain:

$$\rho \left( \frac{\partial \mathbf{u}}{\partial t} + \nabla \cdot \mathbf{u}\mathbf{u} \right) = -\nabla p + \mu \nabla^2 \mathbf{u} + \rho \mathbf{f} \tag{3.31}$$

where $\rho$ is the fluid density and $\mathbf{f}$ is a force per unit volume. In 3.31, the term represented as $\mathbf{E}$ in 3.16 has been written extensively.

The resolutive scheme can be summarized as follows [44]:

$$\mathbf{u}^* = \mathbf{u}^n + \frac{\Delta t}{\rho} \left( -\nabla p^{n-1/2} + \mathbf{RHS}^{n+1/2} \right) \tag{3.32}$$

$$\mathbf{u}^{**} = \mathbf{u}^* + \Delta t \mathbf{f}^{n+1/2} \tag{3.33}$$

$$\nabla^2 \tilde{p} = \frac{\rho}{\Delta t} \nabla \cdot \mathbf{u}^{**} \tag{3.34}$$

$$\mathbf{u}^{n+1} = \mathbf{u}^{**} - \frac{\Delta t}{\rho} \nabla \tilde{p} \tag{3.35}$$

$$p^{n+1/2} = p^{n-1/2} + \tilde{p} \tag{3.36}$$

where $\mathbf{u}^*$ and $\mathbf{u}^{**}$ are the first and second prediction velocities, $\Delta t$ is the computational time step, $\tilde{p}$ is a correction pressure and superscripts denote the $n^{th}$ step of the integration scheme. For the sake of simplicity, the term **RHS** has been introduced and it includes convective and viscous terms.

First prediction velocity $\mathbf{u}^*$ is computed directly from 3.31 without considering IBM forcing term $\mathbf{f}$. Thus, $\mathbf{u}^*$ does not satisfy boundary conditions. The presence of the body is introduced only on $\mathbf{u}^{**}$ and $\mathbf{f}$ must be computed iteratively. This is done by first interpolating the velocity $\mathbf{u}^*$ computed at eulerian nodes on the lagrangian grid solidal to the body. The velocity $\mathbf{U}^*$ obtained in this moving frame of reference is compared to the one of the solid particle $\mathbf{U}_l^n$, allowing for a determination of $\mathbf{f}$. The IBM forcing term is then spread on the eulerian grid in order to satisfy no-slip and no-penetration conditions and the prediction velocity is finally updated. Interpolation and spreading operations are done by mean of a regularized Dirac delta function $\delta_D$.

Better accuracy in the solution can be obtained by an iterative repetition of this process: regularized Dirac delta functions have a finite amplitude so that forcing loads are spread within a radius, characteristic of the particular delta function considered. Areas of influence of near-by eulerian points could then overlap. As a consequence, lagrangian points on the interface can be forced in the same time by different eulerian points, leading to a bad determined forcing term.

The process described above can then be repeated until boundary conditions are satisfied with a certain accuracy, but it is obvious that a higher number of iteration will also increase the computational cost of the process. This forcing scheme can be expressed in mathematical terms as follows [45]-[43]:

$$\mathbf{U}_l^{*,s-1} = \sum_{i,j,k} \mathbf{u}_{i,j,k}^{*,s-1} \delta(\mathbf{x}_{i,j,k} - \mathbf{X}_l^n) \Delta V_e \tag{3.37}$$

$$\mathbf{F}_l^{n+1/2,s} = \frac{\mathbf{U}_l^n - \mathbf{U}_l^{*,s-1}}{\Delta t} \tag{3.38}$$

$$\mathbf{f}_{i,j,k}^{n+1/2,s} = \sum_{l} \mathbf{F}_l^{n+1/2,s} \delta(\mathbf{x}_{i,j,k} - \mathbf{X}_l^n) \Delta V_l \tag{3.39}$$

$$\mathbf{u}_{i,j,k}^{s} = \mathbf{u}_{i,j,k}^{*} + \Delta t \mathbf{f}_{i,j,k}^{n+1/2,s} \tag{3.40}$$

where subscripts $l$ denote quantities computed on the lagrangian grid, superscripts

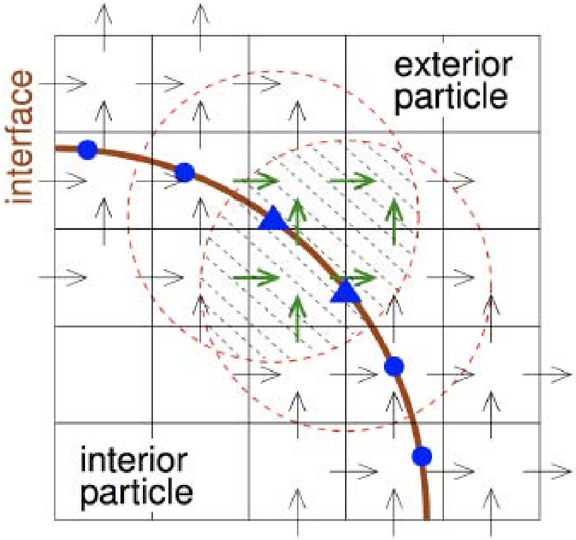

**Figure 3.2:** *Multidirect forcing: circumferences denote the area of influence for each of the lagrangian points marked with a triangle. It follows that all eulerian points in the overlapping region will simultaneously force both these lagrangian points [43].*

$s$ denote the $s^{th}$ iteration of the multidirect scheme, $\Delta V_e$ and $\Delta V_l$ are the volumes for eulerian grid and solid particle respectively.

The forces and torques exerted by fluid and solid onto each other are preserved using the regularized Dirac delta function of Roma et al. [46] during interpolation and spreading. However, this is true only if the spatial resolution of the eulerian grid is uniform in each coordinate direction. For this reason in this framework, fluid domain will be discretized with a uniform element size mesh $\Delta x = \Delta y = \Delta z$.

### 3.3.2 Inward interface retraction

The usage of a regularized delta function for a multidirect forcing scheme like the one described in the previous section, introduces some critical aspects for all lagrangian points on the interface. Indeed, the smooth outer surface of the body is replaced by a thin porous shell of width equal to that of the delta function. For the particular case of delta function in the form of Roma et al., this is equal to $3\Delta x$.

Two effects arise: the first is a direct consequence of the increased size of the body of $3\Delta x/2$, and it is an increase in drag. The second effect, on the other hand, is that porosity is accompanied by a drag reduction, especially when the fluid is in laminar motion near the surface. The predominant effect is the former, so that the overall consequence is of having a body slightly bigger than the original. This fact is mitigated by an inward retraction of all lagrangian points on the surface of the body. The amount of the retraction is such as the computed drag equals the one of the actual body.

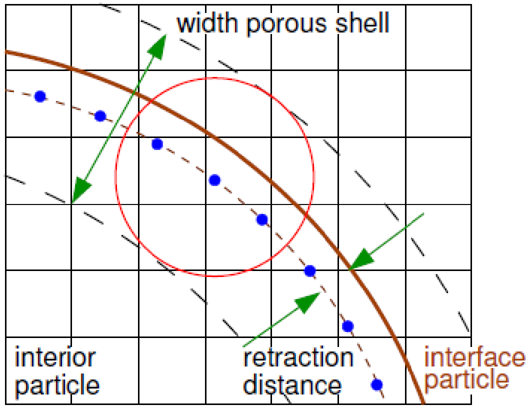

**Figure 3.3:** *Effect of the usage of a regularized delta function. Particle's initial interface is replaced by a porous shell and the effective size of the particle itself is bigger than the original one. This effect is mitigated by a retraction of all lagrangian points on the interface (blue dots) [43].*

# Chapter 4

# Problem definition and approach

This thesis aims to present a study of the interaction between a fluid flow and a solid plate. This is done by mean of a particulary developed code, whose structure is presented in this chapter. In the following, also similarity coefficients to be used within the code and the problem configuration will be presented.

## 4.1 CaNS-ExPS

CaNS-ExPS [33]-[34] is a code especially developed for the solution of FSI problems in which crack propagation is a subject of interest. It is a double precision massively parallelized Fortran code that follows the partitioned approach with a non-conforming mesh method. Numerical techniques embodied are peridynamics for what concerns solid solver, DNS for the fluid flow and IBM for interface conditions. Problems are two-way coupled, meaning that mutual interactions between solid and fluid phases are constantly solved. A validation of all the modules involved has been previously done, as well as of their coupling.

### 4.1.1 Peridynamics module

To solve the equations of motion for a solid medium, the first step is to discretize the body in a set of solid particles of volume $\Delta V$, that overall equate the volume of the body itself. This is done with a structured equispaced grid of constant element size $\Delta x$ such as, in first approximation, $\Delta V = (\Delta x)^3$. Then for the $i^{th}$ node, the equation of motion 3.1 takes the form:

$$\rho_s \ddot{\mathbf{x}}_i^n = \sum_{j=1}^{M} \mathbf{f}(\mathbf{u}_j^n - \mathbf{u}_i^n, \mathbf{x}_j^n - \mathbf{x}_i^n)\beta(\Delta V_j) + \mathbf{b}_i^n \tag{4.1}$$

where the subscript j denotes one of the particles of the neighborhood, whose total number is M and the vector $\mathbf{b_i^n}$ represents the loads applied by the fluid on the surface of the body. Here $\beta$ is a scalar value that is used to correct the volume associated to the $j^{th}$ node. Indeed, a particle has to be considered in equation 4.1 if its distance from the $i^{th}$ node is less than the peridynamic horizon $\delta$. However, particles close to the limit of the horizon, often are not completely inside the area of influence of the particle, and therefore their volume needs to be reduced for a correct solution of 4.1:

$$\beta = \begin{cases} 1 & \text{if } |\xi| < \delta - 0.5\Delta x \\ \frac{\delta + 0.5\Delta x - |\xi|}{\Delta x} & \text{if } \delta - 0.5\Delta x < |\xi| \leq \delta + 0.5\Delta x \\ 0 & \text{otherwise} \end{cases} \tag{4.2}$$

Equation 4.1 is solved by a fully explicit, low storage, third order Runge-Kutta algorithm. The fact that the resolutive method is explicit imposes a boundary on the maximum value for the time step. Indeed in order for the code to be stable, the time step is required to be less than $\Delta t_{max}$:

$$\Delta t_{max} = \frac{|\xi|_{min}}{c_{k,max}} \tag{4.3}$$

where $|\xi|_{min}$ is the minimum size of the bond and $c_{k,max}$ is the maximum sound

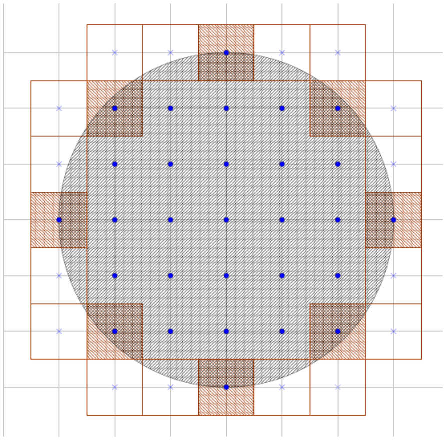

**Figure 4.1:** *Nodes marked with blue dots are those included in the neighborhood, whose area is identified by mean of the black circumference. The volume of the red-colored nodes is not fully inside the circumference and therefore it has to be reduced. On the other hand, nodes marked with a cross are outside of the neighborhood but part of their volume falls inside the circumference [34].*

velocity in the solid medium:

$$c_{k,max} = \sqrt{\frac{E}{\rho_s}} \tag{4.4}$$

The peridynamic solver in the following will be addressed as ExPS (Explicit Peridynamic Solver).

### 4.1.2 Navier Stokes and IBM modules

The flow solver is a further development of open source code CaNS, originally written by P. Costa [47], that has been expanded with the addition of IBM of [43]. Fluid phase has to be fully solved by mean of a DNS, meaning that equations of motion to be solved are 3.15 - 3.31. However, for practical reasons, the solver works in a non-dimensional frame, thus Navier-Stokes equation have to be further developed. Non-dimensional form of these equations is [39]:

$$\nabla \cdot \mathbf{u} = 0 \tag{4.5}$$

$$\left(\frac{\partial \mathbf{u}}{\partial t} + \nabla \cdot \mathbf{u}\mathbf{u}\right) = -\nabla p + \frac{1}{Re}\nabla^2 \mathbf{u} + \mathbf{f} \tag{4.6}$$

in which every entity is now non-dimensional and $Re = \rho u L/\mu$.

Boundary conditions for the fluid field are applied by mean of ghost nodes, or additional nodes external to the computational domain. Dirichlet and Neumann conditions, as well as periodicity, can be imposed both for velocity and pressure. Time integration is achieved by a low-storage third order Rounge-Kutta algorithm while spatial integration by finite differences method.

IBM resolutive scheme is the multidirect forcing scheme described in section 3.3.1.

### 4.1.3 IBM and peridynamics coupling

Main advantage of a partitioned method, see section 2.2, is that fluid and solid solvers work in parallel, independently from each other. However, they need to communicate when updating the position of the lagrangian points and when applying loads conditions on the body. These are directly determined from the solution of solid phase's motion and fluid phase, respectively. Indeed, when solving fluid's equations of motion, IBM treats the body as a set of forces applied at the location of interface lagrangian points in order to satisfy no-slip and no-penetration constraints. These forces, in turn, are the same loads applied to the solid phase and are therefore the input to the peridynamic solver. After solving the equations of motion for solid particles, their new position will be determined and it will directly influence fluid's motion in the next iteration. This way the problem is 2 way coupled.

In a principled way, the modules should be recalled together at every iteration in order to properly describe the problem. However, this way of proceeding could heavily influence the computational efficiency of the code since DNS and peridynamics are both expensive in terms of computational time. The way adopted is to consider 2 different time steps for solid and fluid domain. This way, the solvers are recalled with different frequencies, being their ratio adaptable to the kind of problem studied. By doing so, solid bodies are thought to move and deform following quasi-equilibrium states even if this is not always true. The solution to this problem is achieved with the introduction of a damping factor for velocities in peridynamics equations of motion 4.1:

$$\rho_s \ddot{\mathbf{x}}_i^n = \sum_{j=1}^{M} \mathbf{f}(\mathbf{u}_j^n - \mathbf{u}_i^n, \mathbf{x}_j^n - \mathbf{x}_i^n)\beta(\Delta V_j) - c(\mathbf{u}_i^n - \mathbf{u}_{avg,i}^n) + \mathbf{b}_i^n \tag{4.7}$$

where $\mathbf{u}_{avg,i}^n$ is the averaged velocity of the particles within the neighborhood of particle $i$.

The damping factor $c$ helps peridynamic particles to move by states of equilibrium, although its determination is not easy and it influences the overall solution to the problem. The aspects that have to be considered during the determination of its value, as well as that of the frequencies with which the solvers are used, are the temporal scale of the problem and the phenomena in which the user is interested. Indeed, the addition of a damping term will surely neglect high frequencies vibrations in the solid phase over a threshold value. This could represent a problem for acoustic studies but, for non-acoustic applications such as the one described in this framework, this effect is negligible. Indeed, incompressible fluid solvers would not solve the equations for the propagation of mechanical waves. As a consequence it becomes useless to solve high frequencies vibrations in the body, since they can not be transmitted to the flow.

### 4.1.4 Loads and displacement transmission

Particular attention must be paid on how the peridynamic and fluid modules have to communicate between them. Indeed, they can not directly exchange informations since fluid phase is solved in a non-dimensional form while peridynamics has to be dimensional. This issue is solved by scaling IBM loads and displacements. Scaling factor for IBM forces can be obtained from the dimensional IBM equation 3.31. This can be non-dimensionalized by relating all dimensions involved to their characteristic ones, denoted in the following with the subscript 0:

$$\frac{U_0}{T_0}\frac{\partial \mathbf{u}}{\partial t}+\frac{U_0^2}{L_0}\nabla\cdot\mathbf{uu}=-\frac{p_0}{L_0\rho_0}\nabla p+\frac{\nu U_0}{L_0^2}\nabla^2\mathbf{u}+F_0\mathbf{f} \tag{4.8}$$

and since:

$$T_0=\frac{L_0}{U_0} \qquad\qquad p_0=\rho_0 U_0^2 \tag{4.9}$$

it follows that:

$$\frac{\partial \mathbf{u}}{\partial t}+\nabla\cdot\mathbf{uu}=-\nabla p+\frac{1}{Re}\nabla^2\mathbf{u}+\frac{F_0 L_0}{U_0^2}\mathbf{f}. \tag{4.10}$$

From a comparison between 4.10 and 4.6, it is noted the only difference concerns the additional forcing term **f**. Since it actually represents an acceleration (i.e. a force per mass unit), the dimensionalizing factor $f^*$ can be easily derived:

$$f^*=\rho_0\frac{U_0^2}{L_0}. \tag{4.11}$$

This is the factor that allows to apply IBM forces computed in a non-dimensional frame as load conditions **b** in the dimensional peridynamic formulation:

$$\mathbf{b}_i=f^*\mathbf{f}_{IBM}. \tag{4.12}$$

In a similar way, the scaling factor to be used for displacements is easy to find. Consider a body in which the nodes of the lagrangian grid coincide with the peridynamics particles; Then, displacements will be translated in a non-dimensional form simply scaling for the reference length $L_0$. Thus:

$$\mathbf{x}_i = \frac{\mathbf{X}}{L_0} \tag{4.13}$$

From what has been said, it follows that for a given geometry fluid phase and interface conditions depend only upon some characteristics dimensions: Re, $L_0$, $U_0$, $\rho_0$. The peridynamic module works in a similar way and it is therefore possible to identify the only physical dimensions needed to completely define the problem. These are the material characteristics E, $\rho_s$, $G_0$.

## 4.2 Dimensional analysis and similarity

Just like it has been done for Navier-Stokes equations, also peridynamics equations can be non-dimensionalized in order to describe the solution of the problem starting from some characteristic scaling groups. This procedure helps to define similarity properties, which are useful to reduce computational time [48]. Rewriting equation 4.7 and relating all dimensions to their characteristic ones:

$$\rho_s \frac{U_0^2}{L_0} \ddot{\mathbf{x}}_i^n = \sum_{j=1}^{M} \frac{E_s}{L_0} (\mathbf{f} \beta \Delta V_j) - \rho_s \frac{U_0^2}{L_0} c(\mathbf{u}_i^n - \mathbf{u}_{avg,i}^n) + f^* \mathbf{b}_i^n \tag{4.14}$$

where all entities are now non-dimensional and the previously determined scaling factor $f^*$ has been used for the definition of external applied loads (i.e. IBM non-dimensional loads). For the sake of clarity, the argument of the PW force function has been omitted in this formulation. After some simple mathematical steps, equation 4.14 leads to:

$$\ddot{\mathbf{x}}_i^n = \sum_{j=1}^{M} \frac{E_s}{\rho_s U_0^2} (\mathbf{f} \beta \Delta V_j) - c(\mathbf{u}_i^n - \mathbf{u}_{avg,i}^n) + \frac{\rho_f}{\rho_s} \mathbf{b}_i^n \tag{4.15}$$

In this last equation, only 2 characteristic groups can be identified and they are the ones that allow for the dimensionalization of the solution. Therefore, similarity in the peridynamic module itself is achieved if these 2 groups are kept constant.

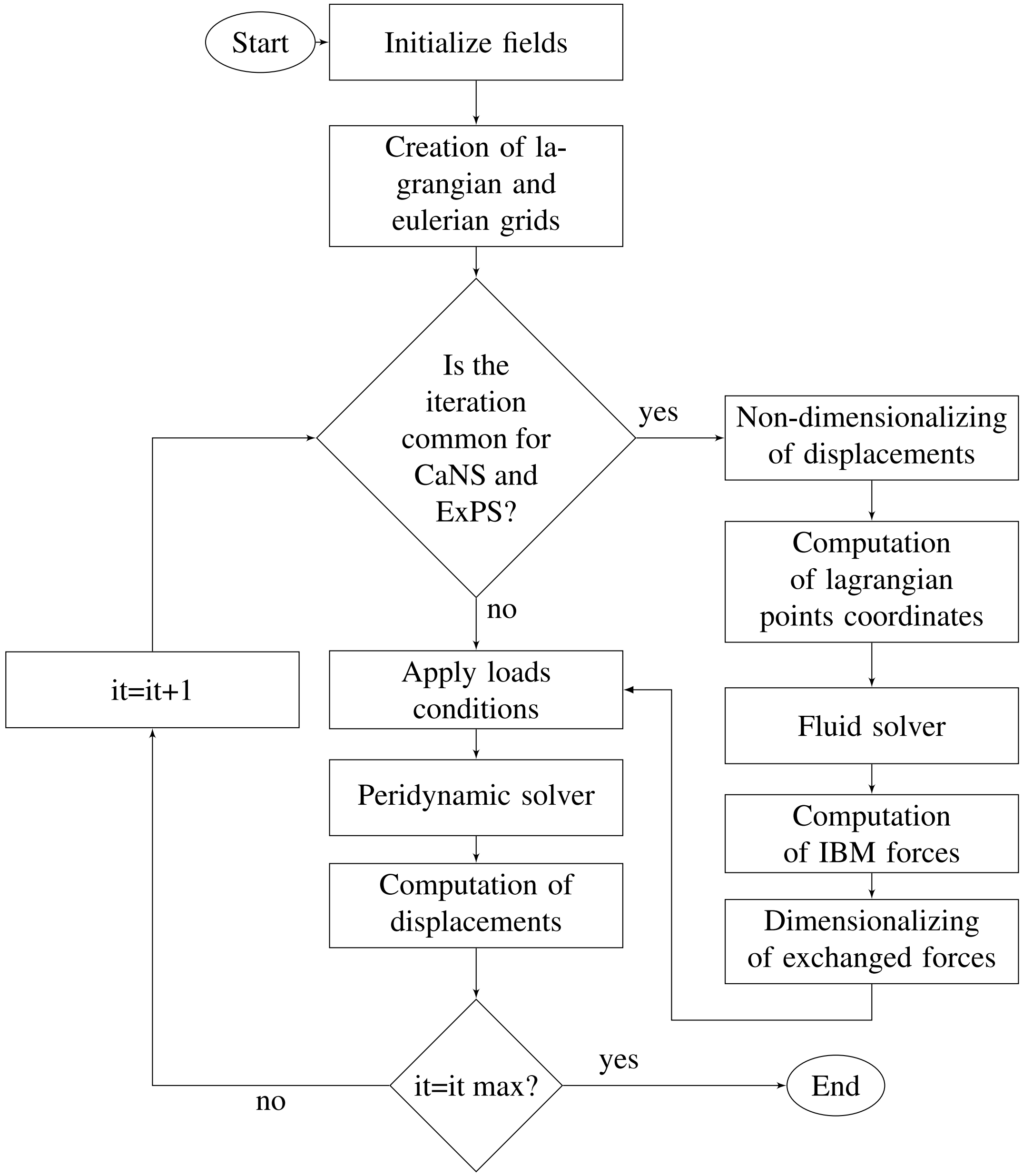

**Figure 4.2:** *Flowchart of the code after the coupling of fluid and solid solvers*

As for the fluid flow and IBM module, non-dimensional Navier-Stokes equations are solved and it is well known that fluid similarity depends only upon

Reynolds number $Re$. In this context, computed IBM forcing are non-dimensional and they are consequences of $Re$ too. IBM forces and external loads $\mathbf{b}_i^n$ in equation 4.15 are the same. Scaling factor $f^*$ is therefore used only to allow for a communication between the modules in this particular code and it is not a characteristic parameter of this kind of problems.

In conclusion, it follows that similarity for FSI problems is based on the equivalence of the following non-dimensional groups:

$$Re = \frac{\rho_f U_0 L_0}{\mu}, \qquad \Phi_2 = \frac{E_s}{\rho_s U_0^2}, \qquad \Phi_3 = \frac{\rho_f}{\rho_s}. \tag{4.16}$$

If these 3 groups are kept constant while geometric similarity is satisfied as well, the solutions of the problem will not vary.

This aspect is greatly useful, especially for the code used in the present framework. Indeed, peridynamics and DNS are 2 heavily expensive computational techniques and the fact that they have been implemented following an explicit approach limitates the maximum allowable time step, as previously said. Acceptable time steps are limited by Young's modulus $E_s$ and therefore realistic materials with $E_s$ of the order of $1e+9Pa$ become nearly impossible to simulate for extensive domains. The issue is solved using fake materials with much lower $E_s$ and similarity.

An example of the application of similarity principle is showed in figures 4.3 - 4.4 where identical results are obtained from 2 different simulations run with CaNS-ExPS code while keeping the aforementioned non-dimensional groups constant. The main difference is about the Young's modulus of the material, equal to $E_1 = 70e+9Pa$ in the first case, and $E_2 = 70e+1Pa$ in the second one.

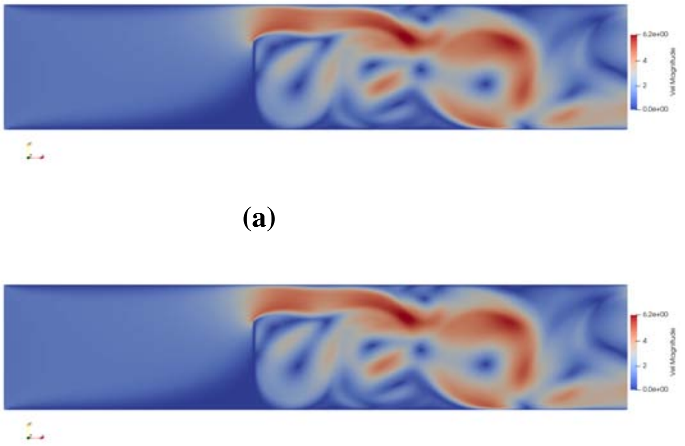

**(a)**

**(b)**

**Figure 4.3:** *Fluid flow in a channel with a vertical plate perpendicular to the flow direction, solved for different reference dimensions and different material properties. Since similarity groups* $Re, \Phi_2, \Phi_3$ *are kept constant between the 2, once the solutions are dimensionalized, obtained results are the same.*

## 4.3 Problem definition and configuration

The present study wants to focus on the mechanics of the erosion of an elastic wall due to its interaction with a turbulent channel flow. The geometry of the problem is kept as simple as possible in order to contain the computational cost in a first approach.

The flow studied is a fully developed turbulent channel flow driven by a stream-wise mean pressure gradient.

Following the nature of the problem, the overall computational domain shall include fluid's computational domain as well as solid's one. The size of the turbulent channel at initial configuration is $6h$ x $3h$ x $2h$ in stream-wise, span-wise and wall-normal direction respectively. The elastic wall is at coordinate $z = 0$ and it is included in the simulation as a plate of the same extension of the channel and thickness $0.250h$. The overall computational domain has thus an extension of $6h$

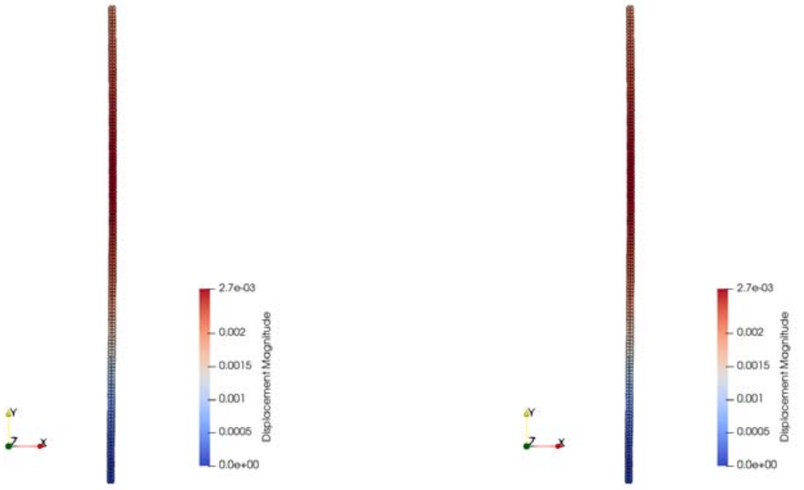

**(a)** **(b)**

**Figure 4.4:** *Detail of the peridynamics solution for the same FSI problem of the previous figure.*

x $3h$ x $2.250h$ and it is dicretized with an eulerian grid of 288 x 144 x 108 nodes.

Since the lagrangian grid, solidal to the body, is required to have a spacing comparable to that of the eulerian grid, it is therefore made up of 288 x 144 x 12 nodes. Grid spacing is $1.04e-2$ for both solid and fluid grids.

Boundary conditions for the flow are no-slip and no-penetration at the upper rigid wall and periodicity in stream-wise and span-wise directions. Fluid flow is driven by a pressure gradient in the stream-wise direction, in order to avoid dissipation due to friction with the walls of the channel to stop the flow. Also peridynamics is periodic in x and y directions. This way the domain is thought to extend indefinitely in these directions. Additional boundary conditions for solid particles are at the lowest limit of the domain, where they are anchored. This condition is achieved by the introduction of 2 more rows of solid particles outside of the computational domain, for which:

$$u_x = u_y = u_z = 0. \tag{4.17}$$

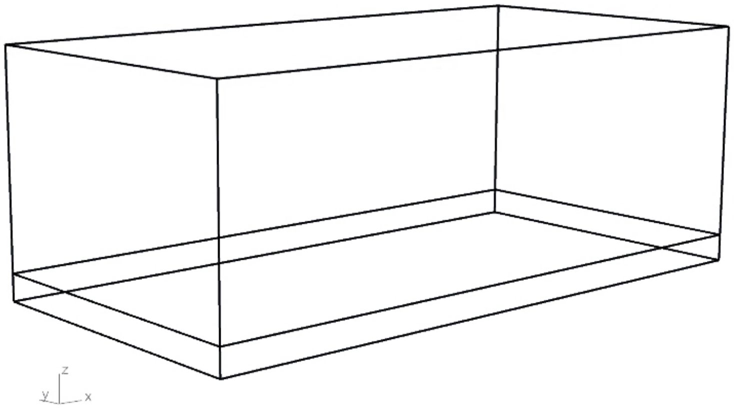

**Figure 4.5:** *Computational domain. The lower zone represent the elastic wall.*

In total, bounded solid particles are 82944.

As for the solid phase, the ratio between the peridynamic horizon and the spacing of the grid is set to $m = \delta/\Delta x = 2$.

Physical parameters required to fully define the nature of the problem are $Re, L_0, U_0, \rho$ (see section 4.2). Their values are contained in table 4.1 together with the material mechanical properties.

| | |
|---|---|
| $Re$ | 4500 |
| $L_0$ | 0.1 m |
| $U_0$ | 0.5 m/s |
| $\rho$ | $1e+3$ kg/m$^3$ |

| | |
|---|---|
| $E$ | $5e+1$ Pa |
| $\rho_s$ | $5e+3$ kg/m$^3$ |
| $G_0$ | $1.32e-3$ J/m$^2$ |
| $c$ | 1000 kg/(m$^3$s) |

**Table 4.1:** *Characteristic physical dimensions of the problem*

It is evident that mechanical properties of the solid phase are highly unrealistic. The choice of such parameters is justified after the considerations made in section 4.2 and helps to contain the computational cost. A more realistic case, whose behavior is the same as the one of the case described in the following, would include fluid and solid in the subsequent table:

|  |  |
|---|---|
| $Re$ | 4500 |
| $L_0$ | 0.1 m |
| $U_0$ | 50 m/s |
| $\rho$ | 1000 kg/m$^3$ |

|  |  |
|---|---|
| $E$ | $5e+5$ Pa |
| $\rho_s$ | $5e+3$ kg/m$^3$ |
| $G_0$ | $1.321e+2$ J/m$^2$ |
| $c$ | 1000 kg/(m$^3$s) |

**Table 4.2:** *Characteristic physical dimensions of a similar problem, in which the solid is characterized by realistic values. Non-dimensional groups Re,$\Phi_2$ and $\Phi_3$ are kept constant between the 2 cases.*

Initial conditions for the flow impose a Poiseuille profile for the stream-wise component of the velocity across the channel, while y and z components follow a sinusoidal law:

$$\begin{cases} u_{x,0}(x,y,z) = 6z(L_z - z) \\ u_{y,0}(x,y,z) = A_y \cos\left(\frac{\pi z}{2}\right) \sin\left(\frac{2\pi y}{L_y}\right) \\ u_{z,0}(x,y,z) = A_z \sin\left(\frac{\pi z}{2}\right) \cos\left(\frac{2\pi y}{L_y}\right) \end{cases} \tag{4.18}$$

where $0 \leq z \leq L_z$ is the wall-normal coordinate in the channel, considered 0 in correspondence of the elastic plate, and $A_y$ and $A_z$ are constants set to 6 and 1 respectively.

This initial velocity profile, together with periodicity conditions, helps to develop a fully turbulent flow, avoiding the risk of vorticity being dumped across the domain. For this reason it is necessary, to dedicate the first iterations to the initialization of the flow, when running the simulation. Peridynamics module will then be switched off during this phase. For this specific case, the first 20000 iterations served this purpose.

# Chapter 5

# Results

As stated above, the solid solver is not used from the very beginning of the simulation when, on the contrary, only the fluid solver is active. This allows for the initialization of a fully developed turbulent flow across the channel. For this particular case, trial simulations showed that 20000 iterations are enough to achieve this condition.

Starting from iteration 20001, both solid and fluid solvers are recalled together as described in the previous chapters and the lower wall of the channel begins to deflect under the effect of the fluid flow. The body is damaged from the loads exerted at the interface that eventually break bonds, gradually increasing damage level for solid particles involved. Rupture first occurs at iteration 33800, when a particle firstly reaches a damage level of $\Phi = 1$.

From this point on, a constantly increasing number of particles is separated from the body as the erosion process continues. The simulation is stopped when the plate is locally eroded for a depth equal to its original thickness, this happening at iteration 45500.

The simulation is complexively made of 45500 iterations, 6800 of which will allow to study the behavior of a flow near an elastic wall and 12500 of which will permit to study erosion.

Results presented in the following are obtained from a single simulation, run

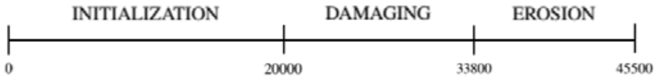

**Figure 5.1:** *Phases in which the overall simulation is divided, together with their relative iterations.*

at MARCONI CINECA using 324 cores. The overall required computational time is of 96 hours, which corresponds to about 31000 core hours.

## 5.1 Results before rupture

### 5.1.1 Fluid domain

Turbulent flows in channels with rigid impermeable walls have been long studied and detailed numerical and experimental results can be easily found in literature [49]-[50]-[51]. Hence, it is reasonable to take them as a reference and to compare results obtained to these, already validated. In particular, mean velocity profiles for turbulent flows follow the so-called law of the wall. It is possible to define $z^+$ and $u^+$ as:

$$z^+ = \frac{u_\tau z}{\nu} \qquad\qquad u^+ = \frac{< u >}{u_\tau} \tag{5.1}$$

They represent the wall-normal distance from the wall and the fluid's velocity parallel to the wall itself in an internal system of coordinates, so that they are dimensionless entities. $u_\tau$ is the shear velocity, computed as:

$$u_\tau = \sqrt{\frac{\tau_w}{\rho}} \tag{5.2}$$

where $\tau_w$ is the wall shear stress.

Expressing $u^+$ as a function of $z^+$ in a turbulent channel, allows to define 3 different layers in the fluid: the viscous sublayer for $y^+ < 5$ where $u^+ = y^+$, the buffer layer, for $5 < y^+ < 30$, where no particular laws exist and the log-law region, for $y^+ > 30$, where $u^+ = \frac{1}{k}\ln y^+ + C$. In the latter expression, $k = 0.41$ is the Von Karman constant and $C$ is a constant set equal to 5.5 for a smooth wall.

First results to be presented concern fluid flow from iteration 27000 to 33000, these being evaluated every 50 iterations. In total, available fields are 120. The time-averaged velocity profile in this particular framework is a function only of wall-distance z. This is true assuming that the mean position of the fluid-solid interface remains fixed over time (i.e. displacements of interface points along z have a mean value equal to 0). It is therefore possible to analyze 2 different aspects for this particular mean velocity profile, whether the origin of the z-axis is set in correspondence of the rigid wall or the elastic one. Figure 5.2 already shows clear non-symmetries in the flow's mean velocity profile, when compared to the mean velocity profile of a turbulent channel flow with rigid walls only, denoted as reference DNS.

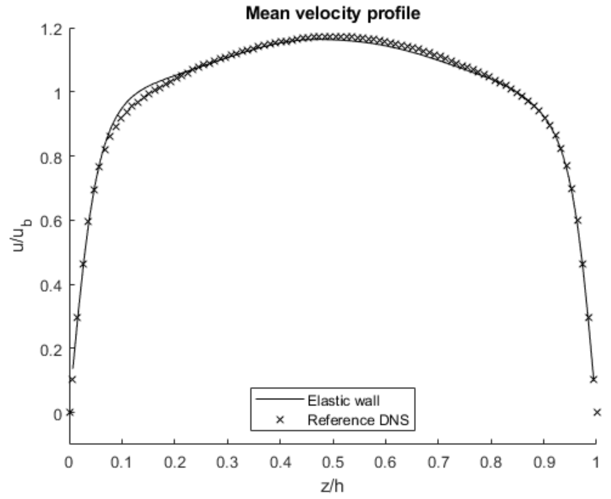

**Figure 5.2:** *Mean velocity profiles for a rigd-elastic wall turbulent channel and for a rigid-rigid wall turbulent channel (cross marked line) as a function of channel position. Velocity and distance are normalized with respect to bulk velocity and channel height respectively.*

It has to be pointed out that the comparison of different results requires them to be normalized. However, for the normalization of coordinates in wall-normal

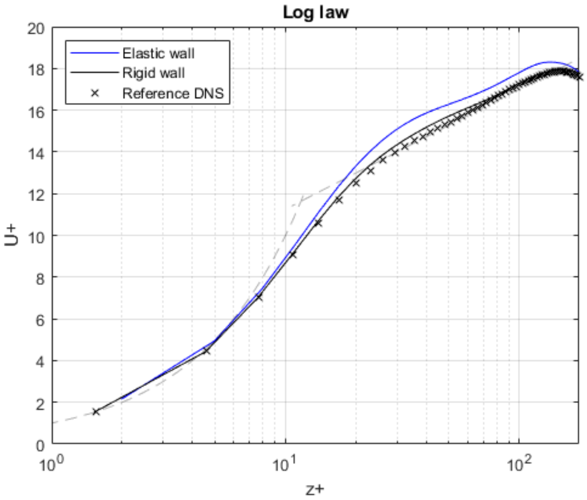

**Figure 5.3:** *Graphical comparison between the mean velocity profile of the fluid flow in a turbulent channel with an elastic wall.*

direction when in presence of an elastic wall, the channel height to be considered is not equal to 1, as it would be expected. Indeed, the inward interface retraction effect described in section 3.3.2 has to be taken into account. In this particular geometry configuration the actual interface is moved $\Delta x/3$ toward the interior of the plate so that the channel height to be considered from now on is: $h_c = 1.0017$. Velocities on the other hand are normalized with respect to the bulk velocity.

Mean velocity profiles in proximity of the rigid impermeable wall and of the elastic one are then computed in terms of $z^+$ and $u^+$. The wall shear stress to be used in the definition of $u_\tau$ in equation 5.2, is the sum of viscous stress $\tau_\mu$ and Reynolds stress $\tau_R$ at the wall:

$$\tau_{\mu,wall} = \mu \frac{\partial < u >}{\partial z}\bigg|_{z=0} \tag{5.3}$$

$$\tau_{R,wall} = -\rho < u'w' >|_{z=0} \tag{5.4}$$

$$\tau_w = \tau_{\mu,wall} + \tau_{R,wall}. \tag{5.5}$$

It is noticeable that $\tau_{R,wall} = 0$ when dealing with rigid walls, since no-slip and no-penetration constraints have to be respected and the wall is fixed in time. On the other hand, it assumes a finite value when it is computed near an elastic, and thus moving, wall.

Results are graphically presented in figure 5.3. In the same figure, a more common mean velocity profile for a turbulent channel flow with only rigid walls (cross marked line) is also presented. This last one is computed from an additional DNS at the same Reynolds number and with the same spatial discretization. This case, denoted in the following as reference DNS, shows perfect accordance with predicted results. The case for $z = 0$ at the rigid wall also shows good accordance to the predicted trend, showing only a slight difference in the buffer layer, where the curve overshoots the expected one.

Major differences concern the case of the origin of axis at the elastic wall. Here, the computed velocity is generally greater than the predicted one. This can be easily seen in figure 5.2 but it appears even more clear in figure 5.3 where it is evident both in the buffer layer and in the loglaw region. This suggest a drag reduction when in presence of an elastic wall, while the flow near the rigid wall remains undisturbed.

At this purpose, an analysis of stresses within the fluid has been carried out and results are shown in figure 5.4. Here, Reynolds stress $\tau_R$, viscous stress $\tau_\mu$ and total shear stress have been computed across the channel and they are normalized with respect to the total shear stress in correspondence of the rigid wall. It turns out that effectively, the total shear stress in correspondence of the elastic wall is less than that at the rigid wall, being:

$$\frac{\tau_{w,elastic}}{\tau_{w,rigid}} = 0.96 \tag{5.6}$$

As a consequence, the location of zero turbulent production (i.e. where shear stresses becomes 0) moves closer to the elastic wall.

Finally, also the diagonal terms of the Reynolds stress tensor have been com-

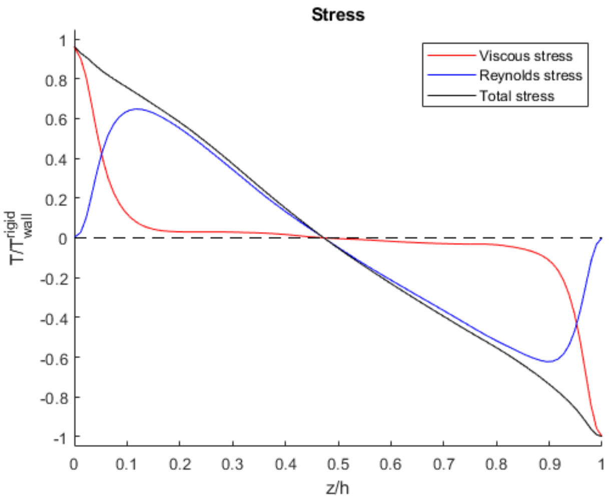

**Figure 5.4:** *Reynolds stress, viscous stress and total shear stress in the channel as a function of wall distance. Both stresses and distances are normalized with respect to rigid wall stress and channel height respectively.*

puted and compared to those of the reference DNS. As it can be seen from figure 5.5, the effect of the elastic wall on turbulence intensities is not limited to the near wall region but, on the contrary, it affects the fluid all over the channel. In particular, stream-wise fluctuations are the most influenced by the presence of an elastic wall. It is interesting to note that for the stream-wise direction, an increase in velocity fluctuations close to the elastic wall is associated to a reduction of fluctuations near the rigid one.

Smaller effect are associated to fluctuations in the span-wise and wall-normal directions.

### 5.1.2 Loads

Until now we mainly focused on the effects of the presence of an elastic wall on the fluid flow. In particular it has been found out that the compliant wall is associated with a reduction in drag and this means that also loads transmitted to the wall will necessary undergo a modification between upper and lower wall of

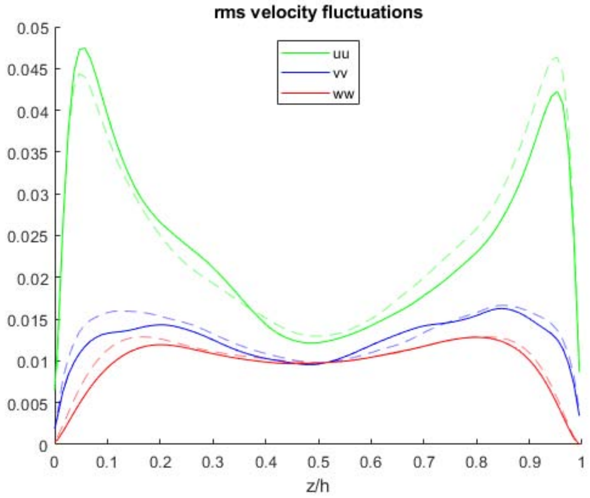

**Figure 5.5:** *Rms of velocity fluctuations. Dashed lines are referred to the reference DNS with only rigid walls.*

the channel. To further analyze this aspect, a detailed study focused on the loads exchanged by fluid and plate has been developed. The way the code is structured allows us to access the exchanged loads for every point of the grid in terms of IBM forcing, which are non-dimensional forces per unit volume. These can then be dimensionalized and associated to stresses (i.e. forces per unit surface) since the spacing of the grids $\Delta x$ is constant in all 3 directions:

$$\tau_{interface} = F_{IBM} \rho U_0^2 \frac{(\Delta x)^3}{(\Delta x)^2} \qquad [Pa]. \tag{5.7}$$

On the other hand, when dealing with rigid walls, boundary forces are not directly given as an output of the code. However, they can be easily estimated with the help of equation 5.3 for stream-wise and span-wise direction.

Again, the previously presented reference DNS has been used at this purpose, over the same time interval to that considered for the FSI simulation. From the former, rigid wall shear stresses have been carried out while IBM forcing at the interface are obtained from the latter. In order to effectively compare wall stresses and find out differences, probability density functions (PDF) and cumulative density functions (CDF) are computed for each case. Obtained results are presented in figure 5.6.

As expected, stream-wise wall shear stresses show a slight reduction for what concerns their mean value when passing from a rigid to an elastic wall. Spectral analysis however, shows that this mean stress reduction is associated to a wider peak distribution. Indeed, rare events have stress magnitudes almost doubled with respect to those in a non-deformable wall. Finally, a particular effect of elasticity in the channel wall is the presence of negative shear stresses in stream-wise direction, not remarkable other way.

As for span-wise wall shear stresses, their mean value remains unchanged and it is equal to 0. PDFs are symmetrical with the only difference that, also in this case, the distribution is wider for the elastic wall case.

In conclusion, it appears evident that an elastic wall is subjected to high magnitude sporadic loads and these rare events are those who will cause the material to get damaged the most.

### 5.1.3 Solid damage

Once the behavior of the fluid flow near the wall and the forces exchanged at the interface are well understood, the way the material breaks has to be investigated. It has however to be noticed that the separation of a particle from the original body is not an instantaneous phenomenon but it follows from a slow and continuous degradation of the material that only in the end is translated into a macroscopic rupture.

This fact is well described by peridynamics, where crack formation is a consequence of subsequent ruptures of bonds. Therefore, from iteration 27000 to 33800, although no macroscopic effects are visible, the wall of the channel is continuously damaged. A quantitative overview of this aspect is derived from the evaluation of damage level for solid material particles.

An *a posteriori* analysis of the problem identifies, by mean of contour plots,

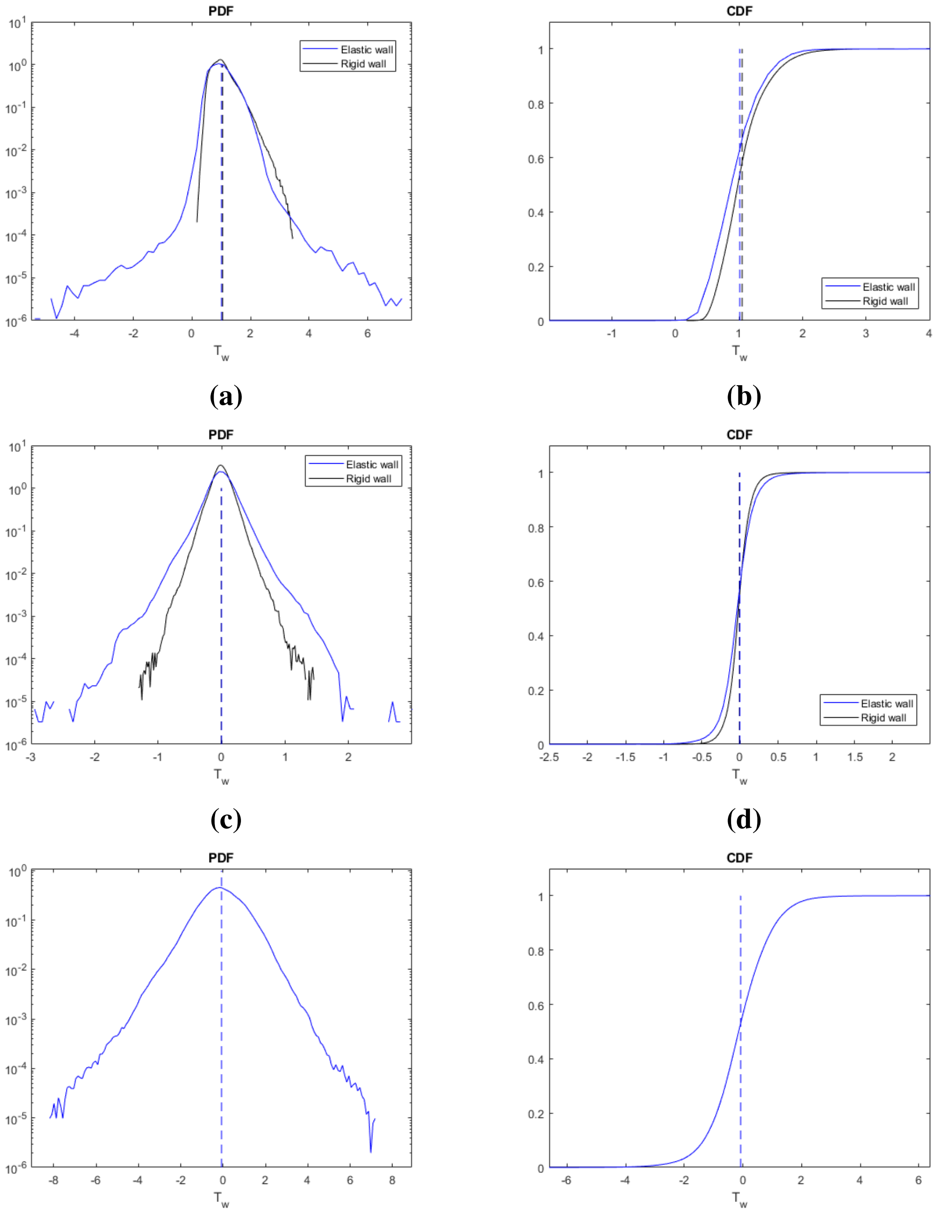

**(a)** **(b)**

**(c)** **(d)**

**(e)** **(f)**

**Figure 5.6:** *PDFs and CDFs of wall shear stresses [Pa] in stream-wise (a - b), span-wise (c - d) and wall-normal (e - f) directions. Dashed lines denote mean values.*

the first surface particle which is separated. This one has to be chosen as the representative one for a significant description of the evolution of the damage process. Figure 5.8 reports the loads magnitudes that the solid particle undergoes as an effect of the fluid flow as a function of time, together with its global damage level. Here, initial time $t = 0s$ is set at the activation of the peridynamic solver so that rupture first occurs at 4.72s, corresponding to iteration 33800 (figure 5.1). As expected from the loads analysis reported in the previous chapter, forces along y and z axis always keep a zero mean value but their amplitude increases as an effect of vibrations of the plate. Indeed, although peridynamic solver is activated at $t = 0s$, it still requires some time for the fluid-plate system to adapt and move freely under the effect of their mutual interaction.

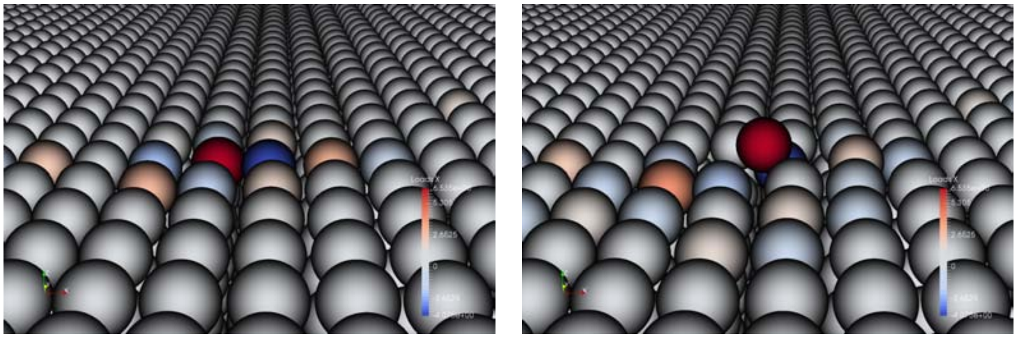

**(a)** $t_1 = 4.32$ **(b)** $t_2 = 4.69s$

**Figure 5.7:** *Detailed view of damage level for material points at iterations near to 33800, when the first particle reaches a damage level* $\Phi = 1$.

On the other hand, force magnitude in stream-wise direction shows a clear increment as the particle stops to communicate with its neighbors and the damage level increases. This is due to the dynamic of the breakage of the particle (figure 5.7), as well as to the fact that when in virgin conditions, the material point redistributes all applied loads to the particles in its neighborhood. However, as degradation starts and bonds break, forces have to be redistributed only along remaining bonds. As a consequence, the load carried by the considered particle alone increases and causes the breakage of even more bonds under a chain effect.

It is because of this fact that forces along x axis and damage level both show an exponential-like trend.

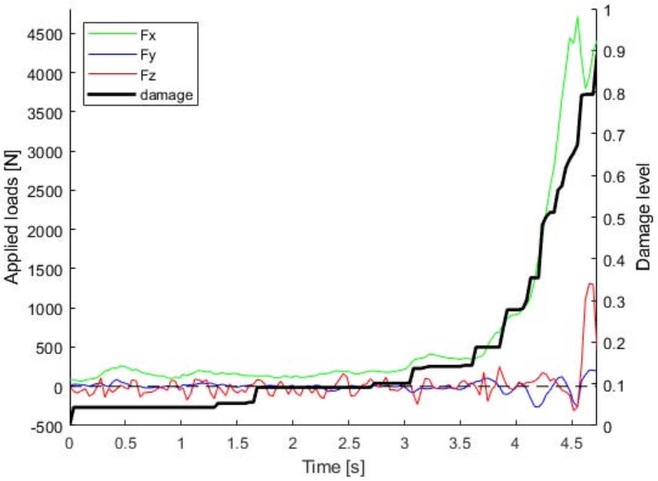

**Figure 5.8:** *Time evolution of forces applied to the first solid particle to break, decomposed along the axis. The black curve represent the damage level of the particle, whose values are printed on the right y-axis.*

The overview of the applied forces itself is not sufficient to determine whether the elastic wall will break in shear or, more in general, what are the mechanics behind rupture. Indeed, since peridynamics deals with fracture only in terms of relative displacement and energy release rate, no informations and distinctions about the fracture mode are given in a principle way. However, results clearly show that bonds that initially break are those in diagonal with respect to the direction of the flow. This can be stated after considering a frame of reference centered on a material point. When a bond breaks, the relative position of the correspondent particle is registered and it is plotted in figure 5.9. This is done for all lagrangian points at the interface of the fluid-solid domain (i.e. on the upper surface) and iterations considered for this purpose are 27000 to 28000. As a result, it is possible to say that these are the initial phenomena that lead to fracture formation and therefore, erosion will begin as a shear fracture.

The consideration of bonds individually introduces another great advantage

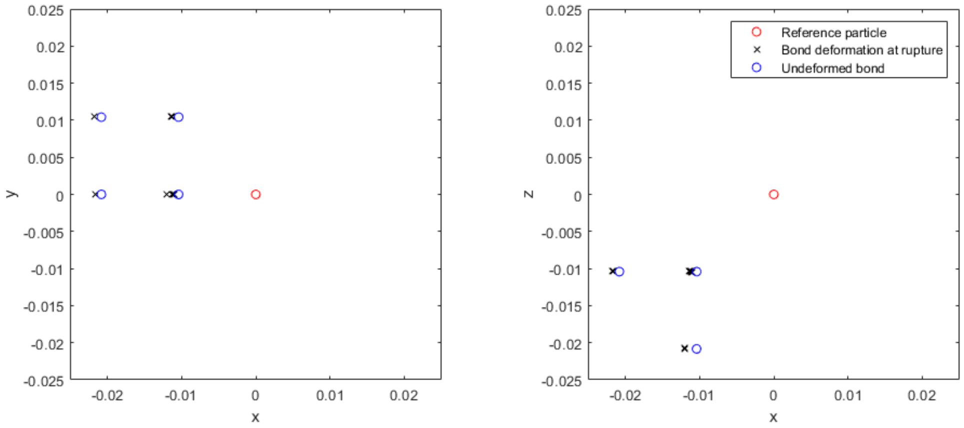

**(a)** **(b)**

**Figure 5.9:** *Graphical representation of the relative position of solid particles when bonds break. Points marked with 'o' denote the position of the particles in the initial configuration, while 'x' is the position they have when the bond breaks.*

once the mode of rupture is determined. Indeed, the knowledge of the relative position of bonds before and after their breakage implies the possibility of a determination of ultimate axial and angular deformations. Averaging those entities for all broken bonds and combining them with the material properties leads to the determination of a shear strength:

$$\tau^* = 1.7160 Pa. \tag{5.8}$$

After the particles represented in figure 5.9 can no more exchange forces along bonds, loads are redistributed to the remaining ones that will eventually break later on. At this point the order in which bonds break becomes more casual and it is determined by fluctuations in the flow and vibrations in the plate.

## 5.2 Results after rupture

After the first particle has reached a damage level $\Phi = 1$, macroscopic effects of the action of the fluid begin to become visible. These are investigated both under a qualitative and quantitative point of view and the results achieved are presented in this chapter.

### 5.2.1 Dynamics of rupture

As the erosion process develops, the number of solid particles removed from the wall constantly increases and surface degradation becomes more relevant. A qualitative overview of the evolution of damage at different times is reported in figure 5.10.

This process is self-powered in a chain effect. Indeed, an extension of what said before allows also for a description of how the whole process evolves. Once the first particle is torn apart by the flow, a lot of other bonds will already be broken. The material is thus weakened and forces transmitted to the plate can not be redistributed to the neighborhood as they initially were. Consequence of this, just like what happened when a single point was considered (see paragraph 5.1.3), is that loads perceived by particles become greater. This way, new particles reach a unitary damage level so that forces have to be directly applied to points that initially were not in direct contact with the fluid flow. The effect of this process is an heavy weakening of the material that has the overall effect of increasing the erosion velocity.

In figure 5.11 it is plotted the way the erosion process evolves in terms of removed material. The plotted curve shows an exponential-like trend: in a short time erosion massively damages the plate. Indeed, if $4.72s$ are needed to first compromise the surface of the plate, in $\Delta t = 2.7s$ the number of particles eroded is already 1000 and they count up to 48210 by the end of the simulation at time $t = 12.95s$.

The removal of particles under the action of the fluid flow continuously modi-

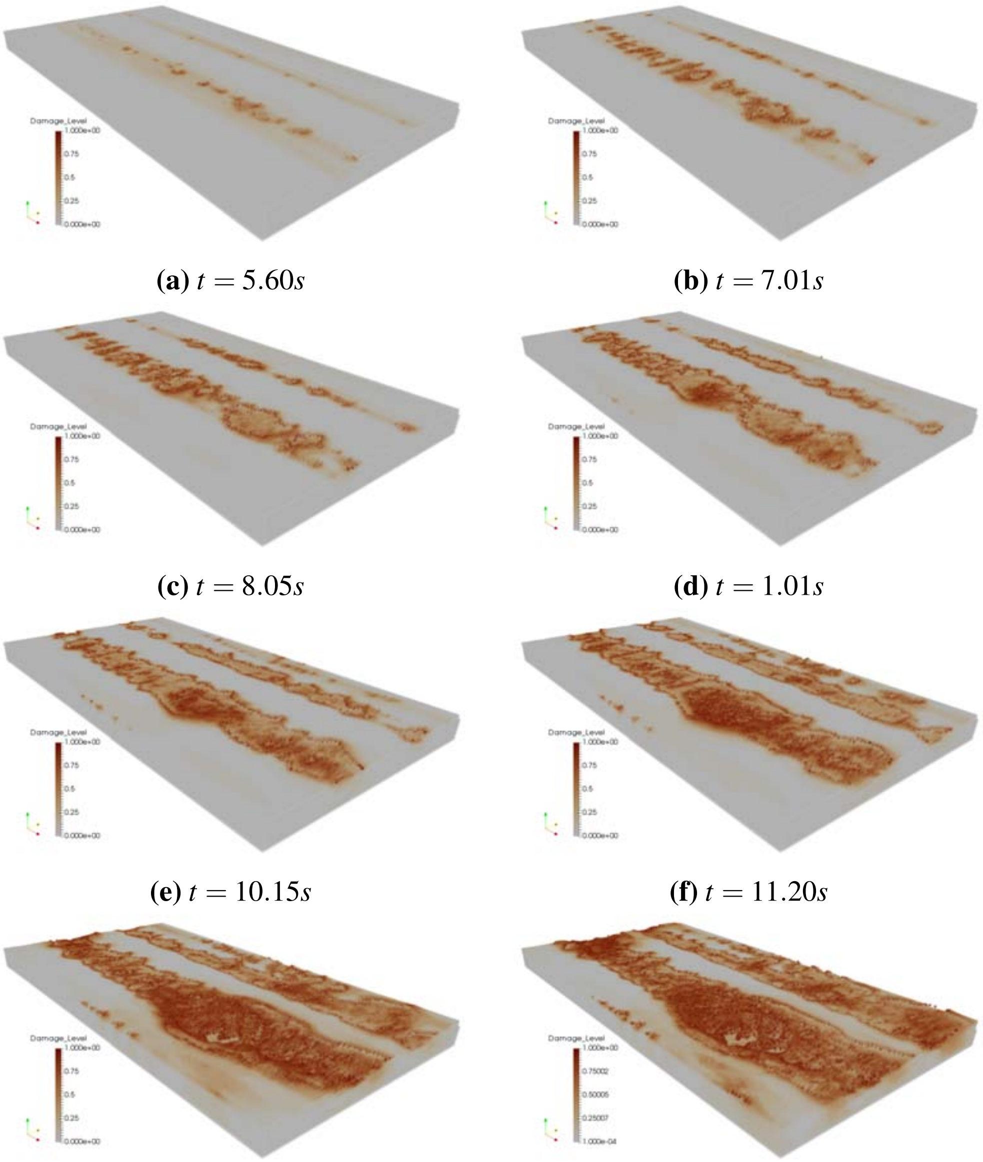

**(a)** $t = 5.60s$ **(b)** $t = 7.01s$

**(c)** $t = 8.05s$ **(d)** $t = 1.01s$

**(e)** $t = 10.15s$ **(f)** $t = 11.20s$

**(g)** $t = 11.90s$ **(h)** $t = 12.60s$

**Figure 5.10:** *Contour plots for the damage level of the plate at different times. All solid particles with a damage level* $\Phi = 1$ *are not plotted for a better representation of the evolution of the eroded surface.*

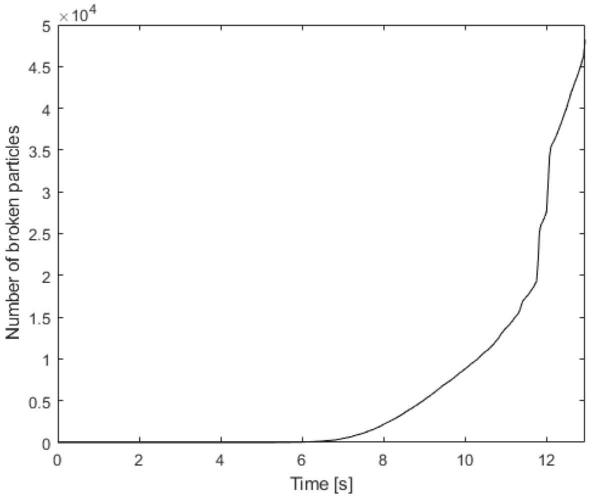

**Figure 5.11:** *Evolution of the erosion of the plate in terms of removed peridynamics particles as a function of time.*

fies the shape of the wall, which initially was flat and smooth. The effect is that the surface becomes rough and therefore, also drag will undergo continuous changes in intensities as the configuration of the interface evolves. Generally, for turbulent flows, roughness translates in a wall shear stress above that of the hydraulically-smooth one. However, since relative roughness is constantly varying, no analytical predictions can be done *a priori*. A computation of mean wall shear stress time evolution, together with their relative maximum and minimum values (figure 5.12), confirms what just said. In particular, it correlates the increase in shear stress with the removal of particles. Until $t = 7s$, when erosion is still in its initial phase and very little damage has been done, wall shear stress averaged on the total surface maintains an almost constant value and roughness effects can therefore be neglected. Mean value begins to increase as the number of particles become relevant and the geometry of the plate is substantially changed. This is accompanied by an augmented spread also between maximum and minimum values.

A graphical overview of the velocity field of the fluid flow, together with results computed for the plate, can justify the rapid increase in the number of eroded

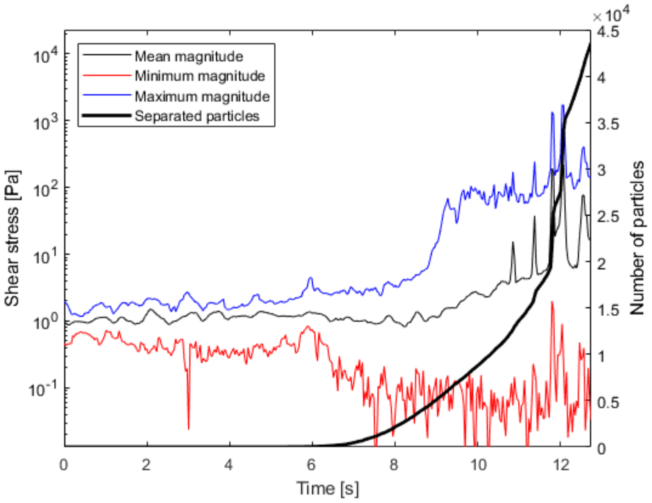

**Figure 5.12:** *Evolution of shear stress exerted by the fluid on the plate as the erosion develops. The line in black represent the spatial averaged value, while the ones in red and the blue the minimum and maximum values respectively.*

particles at $t = 11s$ to $t = 12s$, as well as the peaks for what concerns applied loads. In figure 5.13, attention is posed on the deeper eroded area, which corresponds approximately to $x > 1.7$ and $y < 0.9$. The detachment of particles influences the motion of the turbulent flow. When the depth of erosion reaches a value close to the original plate thickness, the flow occasionally recirculates in the above mentioned zone and interacts with the particles that are washed away. Turbulence is locally increased and high velocity fluctuations occur. The high velocity fluid penetrates between the cavities that formed before, as erosion proceeded. This causes an enormous increase of loads applied to the remaining particles.

Also the presence of the bounded particles pays an important role in the process. Indeed, since all degrees of freedom are locked, displacements can not be transferred to them, making the rupture of bonds easier.

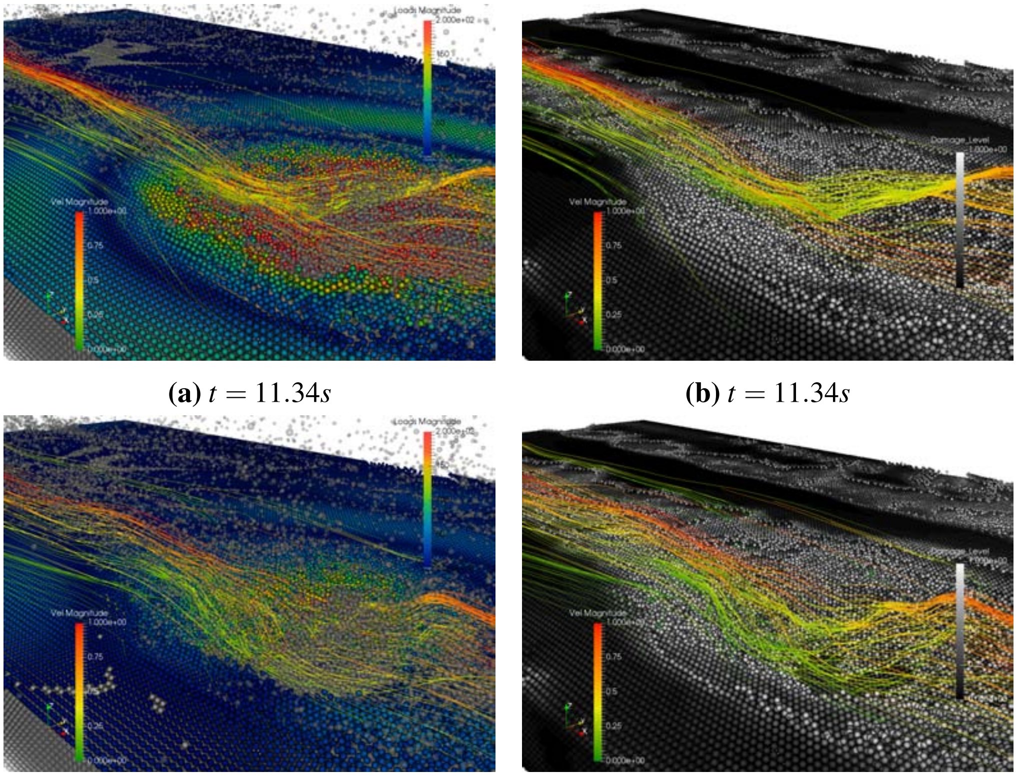

**(a)** $t = 11.34s$ **(b)** $t = 11.34s$

**(c)** $t = 11.90s$ **(d)** $t = 11.90s$

**Figure 5.13:** *Visualization of streamlines in correspondence of the most eroded zone, when the simulation is about to end. Figures a, c, shows the contour plot of load's magnitude. Already eroded particles and the ones underneath the surface, to which zero loads are directly applied, are colored in grey and their opacity is reduced to allow for a better visualization. Figures b, d, on the other hand, show the same time instant and the same streamlines, but the damage level is plotted on the plate. In this case, particles already detached are hidden.*
*In the visualized time instants a large part on the bottom of the plate is removed. This can be easily seen in the right-side column, while on the left-side the increase of loads to cause this event is noticeable*

### 5.2.2 Erosion depth dependence

Studying the evolution of loads by their averaged values is a great instrument but still it does not give any correlation between them and the actual geometry of the plate. Indeed, from figure 5.10 it is clear that geometry is highly irregular and therefore loads distribution can not be uniform on the entire surface.

To overcome this problem and find more information about how the repartition of loads varies with the position, the flat plate is discretized into a $100x30$ grid and results are then averaged on each of these sectors. By doing so, geometry dependence is included in the analysis but still, surface irregularities at smaller scales are smoothed out. While in the previous chapters the plate was considered to remain flat with a thickness equal to its mean one, now the geometry of the plate is derived from the coordinates of each sector.

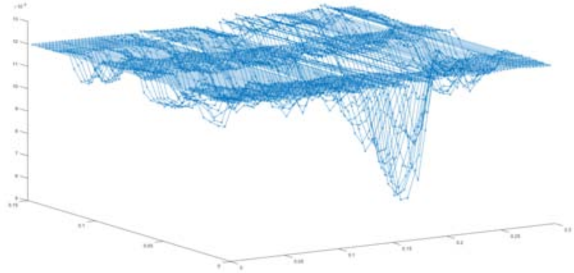

**Figure 5.14:** *Plate discretized in sectors by a 100x30 grid*

Loads transmitted at the fluid-solid interface are then computed at every sector and averaged on it. Mean shear stresses $\tau_x$, $\tau_y$ and normal stresses $\sigma_z$ are associated to the mean thickness of the plate in that particular sector, which is the mean z coordinate of the sector itself. This procedure is done at different time instants, as the erosion proceeds, from that analysis it derives that the increase in applied loads is a direct consequence of the dynamic state of the problem. Indeed, after erosion has started, there is the definition of 2 preferential zones for it to evolves, identified as 2 erosion channels. The one at lower y is eroded much faster than that at higher y where, on the contrary, the process slows down and the erosion seems to be freezed, compared to the other one.

The analysis of loads shows a different behavior for the 2 areas: when the erosion process slows down, transmitted stresses to the eroded zones increase in intensity. For this reason, highest magnitude loads are in correspondence of $z \approx 0.011$, which corresponds to the average depth of the second erosion channel. As for normal stresses, in general, a decrease in thickness is associated to negative, higher magnitude loads (figure 5.15).

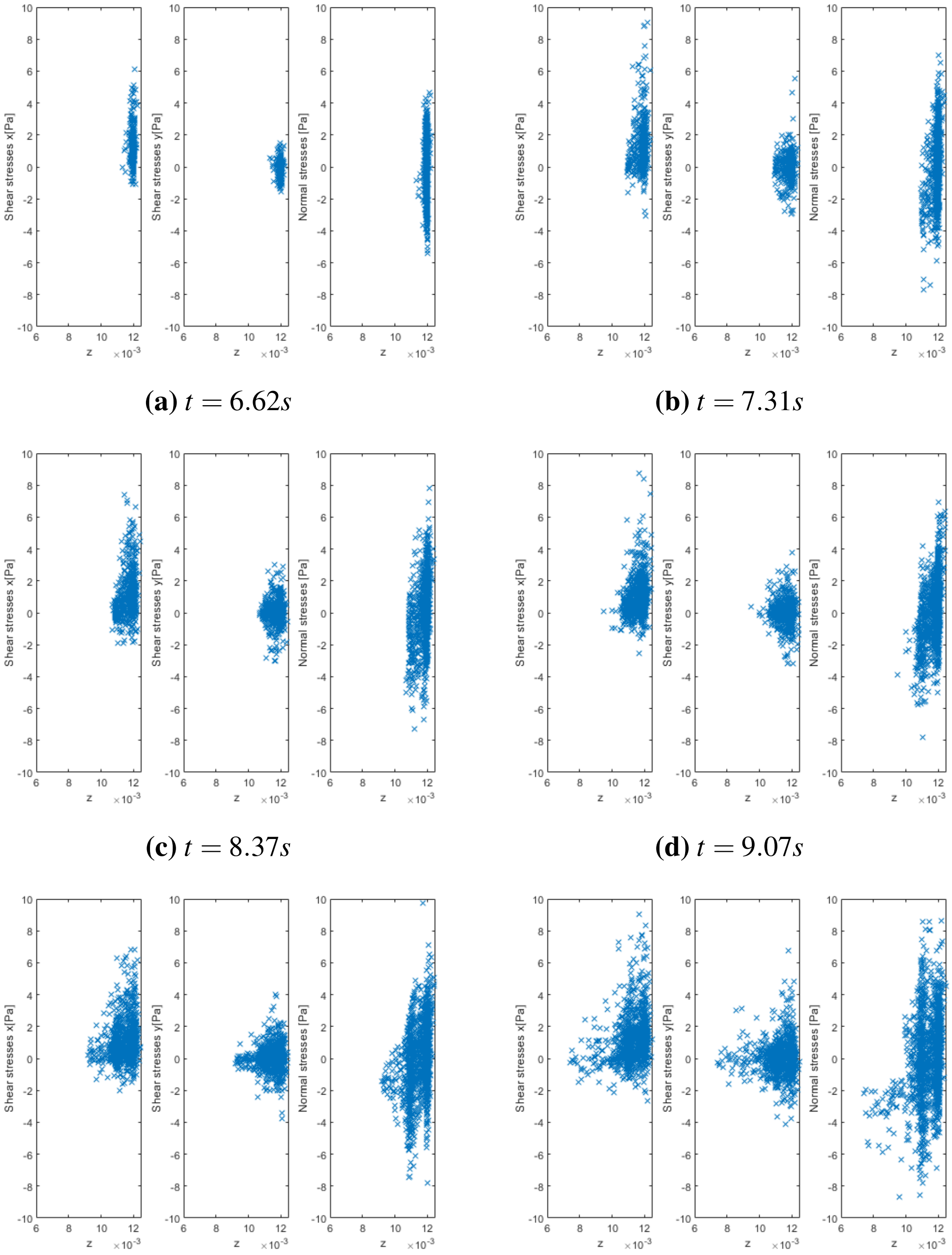

**(a)** $t = 6.62s$ **(b)** $t = 7.31s$

**(c)** $t = 8.37s$ **(d)** $t = 9.07s$

**(e)** $t = 10.96s$ **(f)** $t = 11.52s$

**Figure 5.15:** *Stresses applied on the surface, evaluated at every sector in which the plate is discretized. At each time instant, components of the stresses along the 3 directions are plotted against the z-coordinate of the sector itself. This results in a representation of the evolution of stress distribution as a function of the depth of erosion.*

## 5.3 Erosion law

As it can be seen from the previous chapters, erosion is a process that proceeds in different ways across the body, leading to complex shapes not predictable *a priori*. In particular, once a particle is removed from the flat surface, erosion develops in proximity of this point increasing the size of the damaged area as the simulation continues.

Aspects covered with present work until now are mechanics that drive the erosion of the plate and the process has been treated in terms of forces and removed material. Figures 5.10 and section 5.2.2 show that erosion is not a spatial homogeneous process but, on the contrary, it is strongly related to position and it proceeds with different speeds depending on where attention is payed. If a mean erosion depth had to be computed across the whole plate, no significant results would be achieved. Indeed, the simulation ends when erosion reaches a depth equal to the original thickness of the plate but still there are some spots on it almost unaffected by the process.

In a similar way to what done in the previous section, it is possible to identify different regions of the flat plate where the behavior of the material is kept almost uniform until the end of the simulation and where erosion has removed material evenly across the area. A computation of a localized averaged erosion depth becomes thus significant in these confined zones.

As an example, one of these regions, graphically represented in figure 5.16-a is identified by:

$$1.9 \leq x \leq 2.6 \qquad\qquad 1.2 \leq y \leq 1.5 \tag{5.9}$$

and the time evolution of its height as erosion proceeds is found in figure 5.16-b. It is useful to define an erosion velocity as

$$v_{er} = \frac{\partial h_c}{\partial t} \tag{5.10}$$

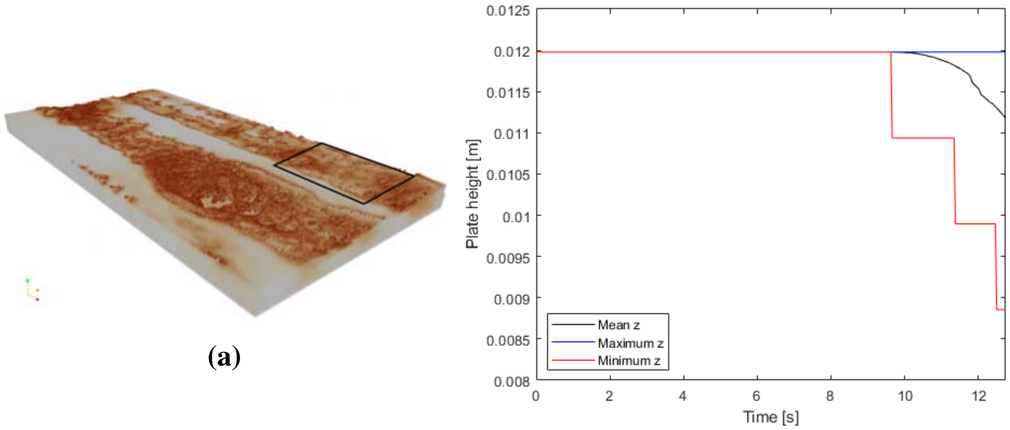

**(a)**

**(b)**

**Figure 5.16:** *Figure a: the area identified by the black line is one of the circumscribed regions where erosion proceeds homogeneously. Figure b: height of the plate in the zone of figure a. The line in black represents the spatial averaged value, while the ones in red and the blue the minimum and maximum values respectively.*

where $h_c$ is the channel height. This height is considered against the plate height $h_p$, since $h_c + h_p = 1.125$ always and in this way erosion velocity assumes only positive values. The erosion velocity in different zones is not constant through all the process but it varies continuously. Considering a mean value for the velocity based on the averaged depth of erosion on each of the sectors defined above, it is possible to obtain the time profile of the erosion velocity. This is, finally, the time derivative of the curve in figure 5.16.

Actually, very little can be derived from such a time evolution. Erosion velocity becomes useful when related to shear stresses applied. The most commonly used erosion law in soil mechanics is:

$$v_{er} = \begin{cases} k_d(\tau - \tau_c) & \text{if } \tau > \tau_c \\ 0 & \text{otherwise} \end{cases} \tag{5.11}$$

with $k_d$ the erosion coefficient expressed in $[m^2 s/kg]$ and $\tau_c$ the critical shear stress, or the minimum shear stress above which erosion begins. The same law is often expressed in terms of rate of removed material $\dot{m}$ so that erosion coefficient in this case is $k_{er} = \rho_s k_d$.

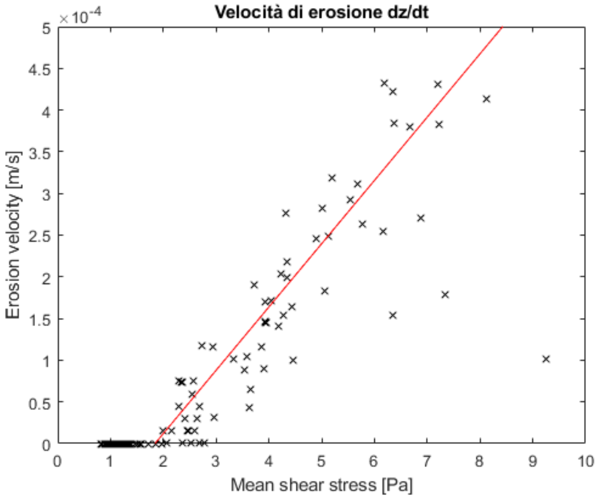

**Figure 5.17:** *Erosion law. Points marked with an x are numerically computed while the line in red is the regression line to fit those values that allows for the determination of $\tau_c$ and $k_d$.*

This relationship between shear stresses and erosion velocity can be verified for the regions of similar behavior. For the same region already represented in figure 5.16-a, obtained results are shown if figure 5.17. The trend is linear and it could be improved with a finer spatial discretization. However results are satisfactory. Computed $\tau_c$, identified as the point where $v_{er} = 0$ on the interpolation line, and the angular coefficient $k_d$ are:

$$\tau_c = 1.84 \pm 0.34 Pa \qquad\qquad k_d = (7.59 \pm 1.95)e - 5\frac{m^2 s}{kg}. \tag{5.12}$$

A comparison between this value for $\tau_c$ and shear strength computed in 5.8 shows good accordance between the two. In this framework, obtained results have to be considered acceptable.

Further improvements of this considerations will be the use of a realistic material in the simulation, whose characteristic parameters $\tau_c$ and $k_d$ are well known in order to have a better confrontation with reality.

# Chapter 6

# Conclusions

The aim of this thesis is the direct study of a FSI problem in which a plate, representation of a wall in a channel, is eroded by a turbulent flow. As for the author knowledge, no previous attempts to directly solve this kind of problem can be found in literature, where on the contrary, this has been done only by mean of models derived from experimental considerations.

The work here presented required the usage of a numerical code especially developed for the solution of similar problems. The approach followed in this code is a partitioned approach because of the possibility of treating solid and fluid phases with two completely different methods. In particular, the chosen methods are peridynamics, for what concerns solid, and DNS and IBM for the fluid phase.

Reasons behind the choose of peridynamics are the intrinsic capabilities of this method to solve fracture and crack propagation without any pregress knowledge on how this is going to evolve. IBM then, allows to easily determine the forces exchanged at the solid-fluid interface in dynamic problems.

The simulation here run required the usage of 2 different grids with the same spatial discretization: the first is fixed in time and concerns the fluid flow, while the other is solidal to the body and is used to solve its equations of motion.

Since the solid solver is built following an explicit approach and maximum allowable time steps are proportional to the elastic modulus of the material, unrealistic properties are assigned to both fluid flow and solid body. This way, the computational time is maintained low. The results here obtained can then be related to a more realistic case thanks to similarity. This is assured thanks to three non-dimensional groups that have to be kept constant.

The presence of an elastic wall in the channel before erosion begins influences directly the behaviors of the flow. In particular it implies a drag reduction in correspondence of the elastic wall with respect to that computed if a rigid wall were considered. Furthermore, the sum of Reynolds stress and viscous stress measured within the fluid in proximity of the elastic wall shows a reduction. This results in a zero turbulence production location closer to the elastic wall. Those effects are confined in a region near the wall. As for turbulence and velocity fluctuations on the other hand, the effect of elasticity can be seen all across the height of the channel.

After focusing on the fluid flow, an analysis of loads transmitted at the solid-fluid interface has been carried out. A comparison between stresses exerted in the elastic and rigid wall cases relates the already mentioned drag reduction to a wider distribution of loads around that value. In particular, the presence of this kind of wall implies higher magnitude loads in rare events. These are responsible for the initialization of erosion, that is a process that follows from a slow and continuous degradation of the material. The way peridynamics is formulated allows for a deep analysis of the mechanics that drive erosion; the body breaks at shear.

The relation between the velocity of erosion derived from the numerical simulation and the shear stresses measured at the surface of the plate showed good accordance to the experimental predicted trend. Finally, the two parameters required for a description of the erosion process for the material here considered have been computed. These parameters can otherwise be derived only from experimental tests.

Results achieved until now are surprisingly good, even considering the small-size domain used. However, during the dissertation, the limitations of the methods used to approach the problem have been identified. A further development of this work is surely to introduce the possibility to simulate realistic materials without the need of similarity. This will also open to the possibility of a comparison between results obtained experimentally and those obtained by a DNS of the same problem.

# Bibliography

[1] "The statistics of embankment dam failures and accidents."

[2] P. D. Boys, "Le rhône et les rivières à lit affouillable," *Annales des Ponts et Chaussées*, vol. 18, pp. 141–195, 1879.

[3] E. Meyer-Peter and R. Müller, "Formulas for bed-load transport," *Proceedings of the Second Meeting of IAHR*, pp. 39–64, 1948.

[4] M. Yalin, *Mechanics of sediment transport*. McGraw-Hill, 1977.

[5] H. A. Einstein, "The bed-load function for sediment transportation in open channel flows," *Technical Bulletin No. 1026, U.S. Departement of Agriculture, Soil Conservation Service,*, 1950.

[6] A. Shields, "Anwendung der aenlichkeitsmechanik und der turbulenzforschung auf die geschiebebewegung," *Mitteilungen der Preussischen Versuchsanstalt fur Wasserbau und Schiffbau*, 1936.

[7] J.-L. Briaud, H. Chen, A. Govindasamy, and R. Storesund, "Levee erosion by overtopping in new orleans during the katrina hurricane," *Journal of Geotechnical and Geoenvironmental Engineering*, vol. 134, pp. 618–632, 2008.

[8] F. Mercier, "Numerical modelling of erosion of a cohesive soil by a turbulent flow," Master's thesis, Aix-Marseille Université, 2013.

[9] I. Vardoulakis, M. Stavropoulou, and P. Papanastasiou, “Hydromechanical aspects of sand production problem,” *Transport in Porous Media*, vol. 22, pp. 225–244, 1996.

[10] D. Lachouette, F. Golay, and S. Bonelli, “One-dimensional modelling of piping flow erosion,” *Comptes Rendus de Mécanique*, vol. 336, pp. 731–736, 2008.

[11] G. Hou, J. Wang, and A. Layton, “Numerical methods for fluid-structure interaction — a review,” *Communications in Computational Physics*, vol. 12, pp. 337–377, aug 2012.

[12] F. Afonso, J. Vale, A. Oliveira, F. Lau, and A. Suleman, “A review on non-linear aeroelasticity of high aspect-ratio wings,” *Progress in Aerospace Sciences*, vol. 89, p. 40.57, 2017.

[13] H. J.-P. Morand and R. Ohayon, “Fluid-structure interaction: Applied numericalmethods,” *Wiley*, 1995.

[14] W. Haase, “Unsteady aerodynamics including fluid/structure interaction,” *Air and Space Europe*, vol. 3, pp. 83–86, 2001.

[15] P. J. Mucha, S. Tee, D. A. Weitz, B. Shraiman, and M. Brenner, “A model for velocity fluctuations in sedimentation,” *Journal of Fluid Mechanics*, vol. 501, pp. 71–104, 2004.

[16] M. Heil and A. L. Hazel, “Fluid-structure interaction in internal physiological flows,” *Annual review of fluid mechanics*, vol. 43, pp. 141–162, 2011.

[17] C. S. Peskin, “Numerical analysis of blood flow in the heart,” *Journal of Computational Physics*, vol. 25, pp. 220–252, 1977.

[18] A. Griffith, “The phenomena of rupture and flow in solids,” *Philosophical Transactions*, vol. 221, pp. 163–198, 1920.

[19] G. Irwin, “Analysis of stresses and strains near the end of a crack traversing a plate,” *Journal of Applied Mechanics*, vol. 24, pp. 361–364, 1957.

[20] D. Dipasquale, M. Zaccariotto, and U. Galvanetto, “Crack propagation with adaptive grid refinement in 2d peridynamics,” *International Journal of Fracture*, vol. 190, pp. 1–22, oct 2014.

[21] R. D. Borst, “Numerical aspects of cohesive-zone models,” *Engineering fracture mechanics*, vol. 70, pp. 1743–1757, 2003.

[22] Y. Mi, M. Crisfield, G. Davies, and H. Hellweg, “Progressive delamination using interface elements,” *J Compos Mater*, vol. 32, pp. 1246–1272, 1998.

[23] J. Munoz, U. Galvanetto, and P. Robinson, “On the numerical simulation of fatigue driven delamination with interface elements,” *Int J Fatigue*, vol. 28, pp. 1136–1146, 2006.

[24] X. J. Z. G. Belytschko T, Chen H, “Dynamic crack propagation based on loss of hyperbolicity and a new discontinuos enrichment,” *Int J Numer Methods*, vol. 58, pp. 1873–1905, 2003.

[25] S. S, “Reformulation of elasticity theory for discontinuities and long-range forces,” *J Mech Phys Solids*, vol. 48, pp. 175–209, 2000.

[26] Y. D. Ha and F. Bobaru, “Characteristics of dynamic brittle fracture captured with peridynamics,” *Engineering Fracture Mechanics*, vol. 78, pp. 1156–1168, 2011.

[27] Y. D. Ha and F. Bobaru, “tudies of dynamic crack propagation and crack branching with peridynamics,” *International Journal of Fracture*, vol. 162, pp. 229–244, 2010.

[28] A. Agwai, I. Guven, and E. Madenci, “Predicting crack initiation and propagation using xfem, czm and peridynamics: A comparative study,” *Electronic Components and Technology Conference*, pp. 1178–1185, 2010.

[29] E. Askari, J. Xu, and S. Silling, “Peridynamic analysis of damage and failure in composites,”

[30] J. Xu, A. Askari, O.Weckner, and S. A. Silling, “Peridynamic analysis of impact damage in composite laminates,” *Journal of Aerospace Engineering*, pp. 21–187, 2008.

[31] B. Kilic, A. Agwai, and E. Madenci, “Peridynamic theory for progressive damage prediction in center-cracked composite laminates,” *Composite Structures*, vol. 90, pp. 141–151, 2009.

[32] G. Zhang, Q. Le, A. Loghin, A. Subramaniyan, and F. Bobaru, “Validation of a peridynamic model for fatigue cracking,” *Engineering Fracture Mechanics*, vol. 162, pp. 76 – 94, 2016.

[33] F. DallaBarba, P. Campagnari, M. Zaccariotto, U. Galvanetto, and F. Picano, “A fluid-structure interaction model based on peridynamics and navier-stokes equations for hydraulic fracture problems,” in *6th European Conference on Computational Mechanics (ECCM 6), 7th European Conference on Computational Fluid Dynamics (ECFD 7)*, 2018.

[34] P. Campagnari, “Studio dell’interazione fluido-struttura con un metodo “immersed boundary” accoppiato alla peridinamica,” Master’s thesis, Università degli Studi di Padova, 2017.

[35] P. S. an M. Parks, “On the role of the influence function in the peridynamic theory,” *Int J Multiscale Computational Engineering*, vol. 9, pp. 689–706, 2011.

[36] S. Silling and E. Askari, “A meshfree method based on the peridynamic model of solid mechanics,” *Computers & Structures*, vol. 83, pp. 1526–1535, jun 2005.

[37] Q. V. Le and F. Bobaru, “Surface corrections for peridynamic models in elasticity and fracture,” *Computational Mechanics*, vol. 16, pp. 1–20, 2017.

[38] K. Yu, *Enhanced Integration Methods for the Peridynamic Theory*. Kansas State University, 2011.

[39] J. Anderson, *Fundamentals of Aerodynamics*. McGraw-Hill Series in Aeronautical and, McGraw-Hill Higher Education, 2007.

[40] P. Kundu, I. Cohen, and D. Dowling, *Fluid Mechanics*. Science Direct e-books, Elsevier Science, 2012.

[41] S. B. Pope, *Turbulent Flows*. Cambridge University Press, 2000.

[42] C. S. Peskin, "Flow patterns around heart valves: A numerical method," *Journal of Computational Physics*, vol. 10, no. 2, pp. 252 – 271, 1972.

[43] W.-P. Breugem, "A second-order accurate immersed boundary method for fully resolved simulations of particle-laden flows," *J. Comput. Phys.*, vol. 231, pp. 4469–4498, 2012.

[44] P. Wesseling, "Principles of computational fluid dynamics," *Springer series in computational mathematics*, vol. 29, 2000.

[45] M. Uhlmann, "An immersed boundary method with direct forcing for the simulation of particulate flows," *Journal of Computational Physics*, vol. 209, no. 2, pp. 448 – 476, 2005.

[46] A. M. Roma, C. S. Peskin, and M. J. Berger, "An adaptive version of the immersed boundary method," *Journal of Computational Physics*, vol. 153, no. 2, pp. 509 – 534, 1999.

[47] P. Costa, "A fft-based finite-difference solver for massively-parallel direct numerical simulations of turbulent flows," *Computers and Mathematics with Applications*, vol. 76, pp. 1853–1862, 08 2018.

[48] A. Casaburo, G. Petrone, F. Franco, and S. De Rosa, "A Review of Similitude Methods for Structural Engineering," *Applied Mechanics Reviews*, vol. 71, 06 2019. 030802.

[49] J. Kim, P. Moin, and R. Moser, “The turbulence statistics in fully developed channel flow at low reynolds number,” *Journal of Fluid Mechanics*, vol. 177, 05 1987.

[50] L. Keirsbulck, L. Labraga, and M. G. el Hak, “Statistical properties of wall shear stress fluctuations in turbulent channel flows,” *International Journal of Heat and Fluid Flow*, vol. 37, pp. 1 – 8, 2012.

[51] H. Abe, H. Kawamura, and H. Choi, “Very large-scale structures and their effects on the wall shear-stress fluctuations in a turbulent channel flow up to re$\tau$=640,” 2004.

[52] N. Benahmed and S. Bonelli, “Investigating concentrated leak erosion behaviour of cohesive soils by performing hole erosion tests,” *European Journal of Environmental and Civil Engineering*, vol. 16, pp. 43–58, jan 2012.